

# Geometrically Induced Selectivity and Unidirectional Electroosmosis in Uncharged Nanopores

Giovanni Di Muccio<sup>1</sup>, Blasco Morozzo della Rocca<sup>2</sup>, Mauro Chinappi<sup>1\*</sup>

<sup>1</sup> *Dipartimento di Ingegneria Industriale, Università di Roma Tor Vergata, Via del Politecnico 1, 00133, Rome, Italy.*

<sup>2</sup> *Dipartimento di Biologia, Università di Roma Tor Vergata,  
Via della Ricerca Scientifica 1, 00133, Rome, Italy.*

(Dated: November 30, 2021)

Selectivity towards positive and negative ions in nanopores is often associated with electroosmotic flow, the control of which is pivotal in several micro-nanofluidic technologies. Selectivity is traditionally understood to be a consequence of surface charges that alter the ion distribution in the pore lumen. Here we present a purely geometrical mechanism to induce ionic selectivity and electroosmotic flow in uncharged nanopores and we tested it via molecular dynamics simulations. Our approach exploits the accumulation of charges, driven by an external electric field, in a coaxial cavity that decorates the membrane close to the pore entrance. The selectivity was shown to depend on the applied voltage and results to be completely inverted when reverting the voltage. The simultaneous inversion of ionic selectivity and electric field direction causes a unidirectional electroosmotic flow. We developed a quantitatively accurate theoretical model for designing pore geometry to achieve the desired electroosmotic velocity. Finally, we demonstrate that unidirectional electroosmosis also occurs for a biological pore whose structure presents a coaxial cavity surrounding the pore constriction. The capability to induce ion selectivity without altering the pore lumen shape or the surface charge paves the way to a more flexible design of selective membranes.

Transport of ions, water, small molecules and polymers through transmembrane protein channels plays a fundamental role in sustaining cellular life and it is drawing increasing attention thanks to the recent progress of nanofluidic technology [1]. High cation or anion selectivity [2], diode-like current rectification [3, 4], different gating mechanisms [5–8], surprisingly large flow rates [9–12] and other unexpected and *exotic* fluid phenomena at the nanoscale were unveiled in the last two decades [13]. This fostered the development of new technological applications based on either biological or synthetic nanopores, such as single molecule nanopore sensing [14, 15] blue energy harvesting [16, 17] and high-throughput biomimetic filters [18].

The coupling of the extreme fluid confinement, geometrical shape and interfacial physico-chemical properties leads to non-trivial electrohydrodynamic phenomena in nanofluidic systems. For example, cation or anion selectivity in nanopores is traditionally understood to be a consequence of charges present on the pore wall. Indeed, electrolyte solution in contact with a charged surface forms an oppositely charged diffused layer, known as the Debye layer, at the solid-liquid interface [19]. Due to the high surface-to-volume ratio, the Debye layer often occupies a non-negligible part of the lumen of charged nanopores. When a voltage is applied across the pore, the total electric current will be mostly formed by the predominant mobile charges (cations or anions) present in the Debye layer, resulting in a selective ionic transport. Moreover, the Coulombic force acting on the net charge of the Debye layer results in a force on the solvent that generates a fluid motion, usually indicated as

electroosmotic flow (EOF). EOF plays a relevant role in nanopore sensing technology since it can compete or cooperate with electrophoresis and dielectroforetic forces acting on the analyte [20, 21] and it can be exploited to capture molecules independently of their charge [22, 23].

Many studies aimed at tuning ionic selectivity and EOF involve the chemical modification of the pore to introduce surface charges [24–26] but other mechanisms have been exploited. An example is provided by externally gated nanopores, where the pore surface charge is controlled via additional electrodes [27–32] applied to the membrane substrate. External gating allows to achieve a good control of the pore selectivity, although the complex fabrication *de facto* limits its application for pores of nanometer or sub-nanometer diameter. Another strategy that can be employed to tune pore selectivity exploits Induced-Charge Electrokinetic (ICEK) phenomena. Differently from externally gated selectivity control, in ICEK the same external electric field that drives the ions through the pore, also polarizes the solid membrane inducing a surface charge that, in turn, alters the Debye layer in the nanochannel and, hence, the selectivity and the EOF [33–35]. A core ingredient to generate a net EOF by ICEK is the presence of some asymmetries in the system that give rise to inhomogeneities of ionic density distributions along the pore in response to the applied voltage. In the nanopore realm, often this asymmetry is introduced in the geometry of the pore (e.g., conical pores [35]) or imposing salt gradients through the membrane [36].

Here, we propose a mechanism to induce a voltage-dependent ionic selectivity and EOF in uncharged cylindrical nanopores by taking advantage of geometrical asymmetries of the membrane without any external voltage-gating control, salt gradient or chemical modifi-

\* mauro.chinappi@uniroma2.it

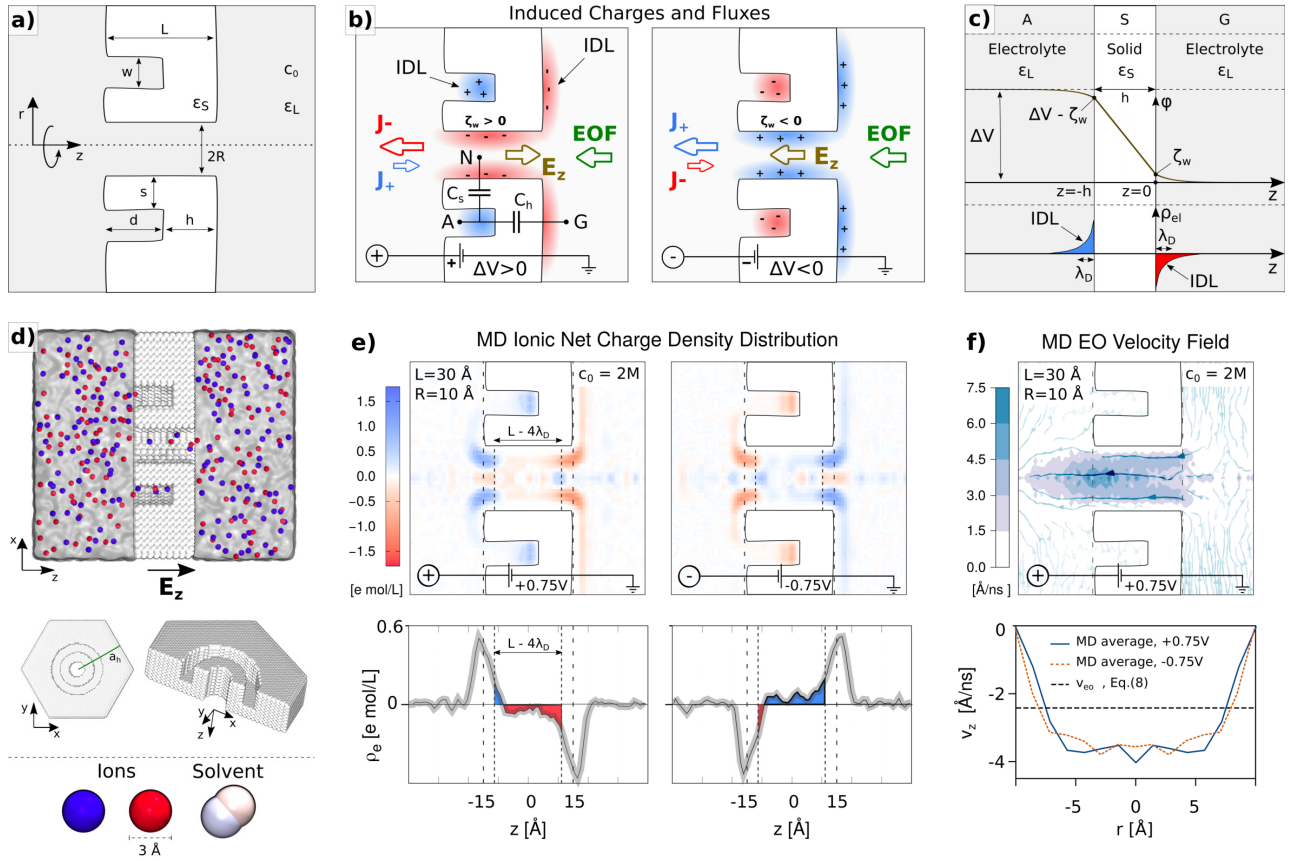


**FIG. 1. Geometrically Induced Selectivity Switch.** **a)** Geometry of the system. A nanopore of radius  $R$  is drilled through a membrane of thickness  $L$ . The channel is surrounded by a coaxial cavity of width  $w$  and depth  $d = L - h$ , at distance  $s$  from the nanopore wall. **b)** Working principle. An external applied voltage  $\Delta V$  gives rise to induced Debye layers (IDLs) at the solid-liquid interfaces, the polarity of which depends on the voltage sign. Meanwhile, the electric field  $E_z$  drives the ions through the nanopore. The presence of a charged IDL inside the nanopore results in a selective ionic transport ( $J_+ \neq J_-$ ), causing an electroosmotic flow (EOF). Since both the electric field  $E_z$  and the selectivity depend on the applied voltage polarity, the EOF (green arrow) is always oriented in the same direction. **c)** Planar electrolytic capacitance. An infinite neutral membrane separates two reservoirs filled by the same electrolyte solution. When a voltage  $\Delta V$  is imposed across the membrane, surface electric potential  $\pm\zeta_w$  arise at the solid-liquid interfaces and charges are accumulated in the IDLs (blue and red areas) whose characteristic size is the Debye length  $\lambda_D$ . **d)** Molecular Dynamics set-up and tilted views of the membrane. White spheres represent the solid membrane atoms, blue and red ones the positive and negative ions, and the transparent gray background the solvent, composed by dipolar diatomic molecules, shown at the bottom. **e)** Charge distribution from MD at  $\Delta V = \pm 0.75$  V, with  $c_0 = 2$  M salt concentration. Bottom plots represent the average net charge density in cylindrical sections of radius  $R = 10$  along the pore axis. Confidence intervals, calculated using a block average with each block corresponding to 10 ns, are reported in shaded gray. **f)** Electroosmotic velocity field from MD at  $\Delta V = +0.75$  V. Bottom panel represents the MD average velocity profile ( $v_z$  component) inside the pore ( $|z| < L/2 - 2\lambda_D$ ) at  $\Delta V = \pm 0.75$  V. The dashed line represents the model prediction, Eq. (8). MD distributions and fluxes are averaged over 800 ns MD trajectory (16 000 frames), see methods.

cation of the pore surface. Our system, Fig. 1b, exploits the accumulation of charge between the pore lumen and a coaxially surrounding cavity. The induced selectivity is completely inverted by reverting the applied electric field. The concurrent inversion of ionic selectivity and applied voltage generates a unidirectional EOF, independently of the applied voltage polarity. We developed a theory, based on a continuum electrohydrodynamical description, to assess the dependence of selectivity and EOF from applied voltage  $\Delta V$  and pore geometry.

As a proof of principle, we set up a molecular dynamics (MD) simulation of a model system composed by an

uncharged solid-state nanopore surrounded by a coaxial cavity, Fig. 1a,d. Our MD results show that the EOF depends quadratically on  $\Delta V$ , in agreement with the theory. We finally demonstrate that selectivity switch and unidirectional EOF also occur for the CsgG bacterial amyloid secretion channel [37, 38], a protein pore employed in a commercial nanopore sequencing device [39] that presents a coaxial cavity as in our simplified model.

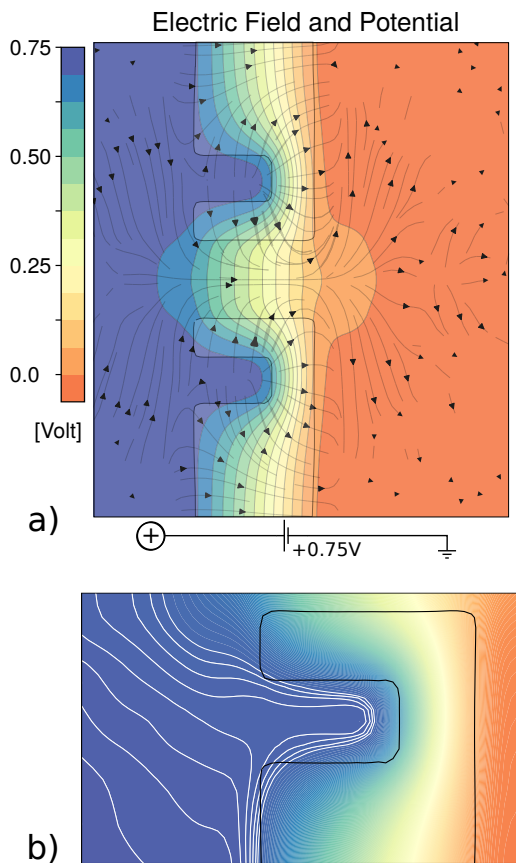


FIG. 2. **a) Electric potential map.** The black arrowed lines represent the electric field  $\mathbf{E}(r, z) = -\nabla V$ . We filtered out the lines where  $|\mathbf{E}(r, z)| < 13\%$  of the maximum intensity. The potential map is averaged over 800 ns MD trajectory (16 000 frames), see methods and refer to the MD simulation of the 2M system shown in Fig. 1d-f, with  $R = 10\text{\AA}$ ,  $L = 30\text{\AA}$ ,  $h = 10\text{\AA}$ ,  $s = 9\text{\AA}$ ,  $w = 12\text{\AA}$  at  $\Delta V = +0.75\text{ V}$  transmembrane applied bias. **b) Zoom on the cavity.** The isolines roughly follow the solid walls, indicating the presence of the induced Debye layer inside the cavity. Selected isolines in the left reservoir were highlighted in white for clarity.

## I. RESULTS AND DISCUSSION

**Geometrically Induced Selectivity Switch: working principle and MD simulations.** Let us consider the system represented in Fig. 1a, composed of a solid insulating membrane (white) of thickness  $L$  with a cylindrical nanopore of radius  $R$ , surrounded by a coaxial cavity of width  $w$  and depth  $d = L - h$ , at a distance  $s$  from the nanopore wall. The membrane (relative permittivity  $\epsilon_S$ ) is immersed in 1:1 electrolyte solution (gray background) with relative permittivity  $\epsilon_L$  and oppositely charged ions with the same ion mobility  $\mu_{\pm} = \mu$ . The pore is completely uncharged, so equilibrium (no applied voltage) ionic concentrations  $c_+$  and  $c_-$  are homogeneous everywhere and equal to the bulk value  $c_0$ . When a voltage  $\Delta V$  is applied across the nanopore, two main effects

occur, as sketched in Fig. 1b; i) ions flow through the pore lumen ( $J_+$  and  $J_-$  arrows) and ii) Induced Debye Layers (IDL) form at the solid walls (blue and red charged clouds), depending on the voltage polarity. The presence of the cavity affects the IDL shape resulting in an accumulation of charges across the cavity and the nanopore lumen, whose signs depend on the voltage polarity, see Fig. 1b. The broken electroneutrality inside the pore results in ionic selectivity (anionic and cationic currents are different) and EOF.

In order to catch the dependence of the pore selectivity on the applied voltage  $\Delta V$  we reasoned as follows. As a first approximation, electrophoretic ionic fluxes are proportional to the concentration and mobility of each species [19],  $\mathbf{J}_{\pm} = \pm \mu c_{\pm} \mathbf{E}$ , with  $\mathbf{E}$  the driving electric field. We use the difference between the cations and anions fluxes as a measure of the ionic selectivity

$$\Delta J = \langle |J_+| - |J_-| \rangle_N \approx \mu \frac{\langle \rho_{el} \rangle_N}{\nu e} |E_z|, \quad (1)$$

with  $\rho_{el} = \nu e(c_+ - c_-)$  the net charge density,  $\nu$  the valence of the ions,  $e$  the elementary charge and where  $\langle \dots \rangle_N$  denotes the volumetric average inside the nanopore. So, selectivity depends on the sign of the charge of the IDL inside the nanopore lumen.

To quantify the IDL in the nanopore, we focus on the positive voltage case of Fig. 1b, left side. A potential difference is present between the lateral cavity (point A at potential  $\Delta V$ ), and the right reservoir of the membrane (point G, grounded), and between the cavity and the pore lumen (point N).

The description of the planar membrane solution is instrumental to understand the IDL dependence on voltage, Fig. 1c. In the right reservoir (G), due to the potential difference ( $\zeta_w$ ) between the bulk and the wall, negative ions accumulate close to the membrane surface, red area. Similarly, positive ions accumulate on the left side (A), blue area. Inside the membrane the electric potential  $\phi(z)$  decays linearly.  $\zeta_w$  is proportional to the applied voltage  $\Delta V$ , see Supplementary Note S1 and Supplementary Fig. S1 for details. Since the accumulated charge in the IDL is also linear in  $\Delta V$ , the process can be described as a capacitance between A and G. Extending this reasoning to our nanopore system, the charge accumulation between the lateral cavity (point A) and the nanopore lumen (point N) can be modeled as a capacitance. Actually, the potential difference between the lateral cavity and the nanopore lumen is a function of the  $z$  coordinates, since the potential inside the pore lumen varies along the nanopore axis. Nevertheless, in a quasi-1D approximation, see Supplementary Note S1, the total charge  $q_N$  inside the nanopore is still proportional to the applied voltage, *i.e.*  $q_N = -C_s \Delta V$ , with

$$C_s = \pi \epsilon_0 \epsilon_S \frac{(L - h)^2}{L \ln(1 + \frac{s}{R})} \frac{L - 4\lambda_d}{L}, \quad (2)$$

an equivalent capacitance between the cavity and the pore that depends only on geometrical parameters.

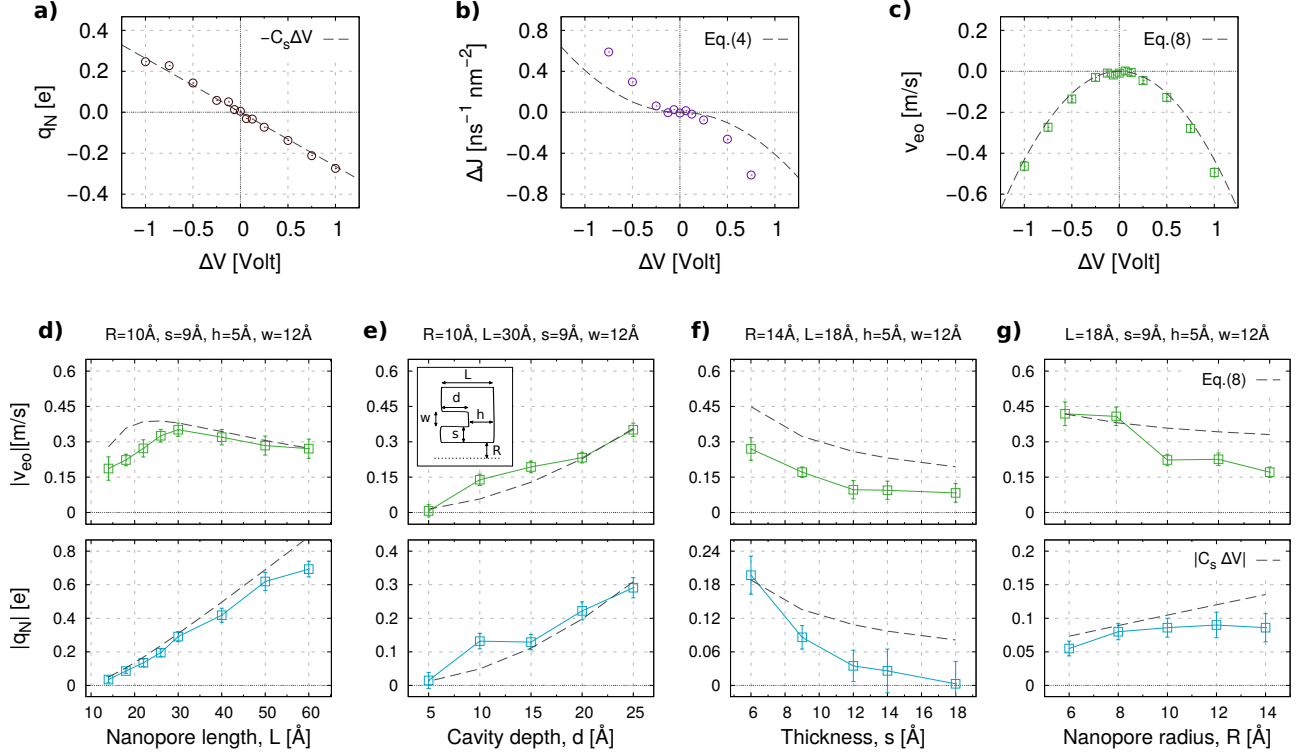


FIG. 3. **Electrohydrodynamic fluxes and charges in the nanopore.** **a-c)** Charge in the pore ( $q_N$ ), selectivity ( $\Delta J$ ) and average EO velocity ( $v_{eo}$ ) from MD simulation of the 2M system shown in Fig. 1d-f, with  $R = 10\text{\AA}$ ,  $L = 30\text{\AA}$ ,  $h = 10\text{\AA}$ ,  $s = 9\text{\AA}$ ,  $w = 12\text{\AA}$ . Dashed lines refer to the analytical model described in the text. **d-g)** Electroosmotic velocity and total charge in the pore as a function of **d)** pore length  $L$ , **e)** depth of the cavity  $d$ , **f)** thickness  $s$  and of **g)** pore radius  $R$ . Analytical model results are shown as dashed lines and MD data as colored squares. Each error bar represents the standard error obtained from an 800 ns MD trajectory (16 000 frames). Inset in **e)** recalls the geometric parameters of our model.

Therefore, the average net charge density inside the nanopore is

$$\langle \rho_{el} \rangle_N = -\frac{C_s \Delta V}{\pi R^2 L}, \quad (3)$$

and, consequently, the ionic selectivity, Eq. (1) reads

$$\Delta J = -\frac{\mu}{\nu e} \frac{C_s |\Delta V|}{\pi R^2 L^2} \Delta V. \quad (4)$$

Eq. (4) shows that selectivity reverts when inverting the applied voltage  $\Delta V$  and its magnitude depends on  $\Delta V$  quadratically.

We tested the above analytical model by using all-atoms molecular dynamics (MD) simulations. To get rid of any asymmetries of the electrolyte that may potentially give rise to competing selectivity of the nanopore (e.g., differences between ion mobilities, different hydration shells around cations and anions, preferential interaction of one ion with the solid) we built a custom symmetric model for the electrolyte solution. In particular, we considered two monovalent ionic species with same mass dissolved in a liquid composed of diatomic dipolar molecules. The membrane is composed by neutral atoms. All the atoms have the same van der Waals radius and

the volume of the solvent molecule is similar to water, see methods for details and Supplementary Fig. S4-S9 for a characterization of the fluid in terms of phase diagram, relative electrical permittivity, wetting, ion mobility and viscosity.

We first studied a system with pore length  $L = 30$ , pore radius  $R = 10$ , cavity width  $w = 12$  and depth  $d = 10$  at distance  $s = 9$ , for a 2M solution Fig. 1d. Ionic net charge densities are reported in Fig. 1e for positive  $\Delta V = +0.75V$  and negative applied voltage  $\Delta V = -0.75V$  showing the formation of IDLs. It is apparent that when a positive voltage is applied, positive charges are accumulated inside the cavity and a corresponding negative IDL arises along the pore. The opposite happens for negative bias. The characteristic length scale of the IDL appears to be, as expected, of the order of the Debye length of the electrolyte solution,  $\lambda_D \simeq 2\text{\AA}$ , in this case. Moreover, liquid velocity profiles show an EOF directed from right to left for both positive and negative voltages, Fig. 1f. The MD simulations revealed additional features of the charge distributions such as the two opposite charge density peaks appearing at the nanopore entrance and discontinuous patterns along the pore axis. Nevertheless, the overall IDL formation mechanism proposed in Fig. 1b is confirmed:

when changing the applied voltage, the selectivity of the pore switches from cations to anions. The electric potential estimated from MD simulation, Fig. 2, further confirms the trends of the voltage drops schematically described in our model. The electric potential decreases quite linearly along the pore, while large part of the cavity is approximatively isopotential with respect to the left reservoir ( $\Delta V = +0.75$  V). More in detail, the isolines follow the wall surface inside the cavity indicating that the IDL contours the wall profile, Fig. 2b.

**Parabolic electroosmosis.** As anticipated in the previous section, a major consequence of the selectivity switch is that the EOF is always negative in our framework (Fig. 1b), *i.e.* directed from the right to left side of the membrane, for both positive and negative voltages. An analytical insight on the dependence of EOF on  $\Delta V$  can be derived using a continuum electrohydrodynamics approach based on the Poisson-Nernst-Planck and Navier-Stokes (PNP-NS) equations [19]. PNP-NS system is derived under several assumptions that are not always respected at the nanoscale, such as the continuum assumption. Moreover, in order to get a practical analytical solution, we needed to rely on several additional hypotheses, such as dilute solution limit and homogeneous mobility. A discussion of these hypotheses and their implications is reported in Supplementary Note S2. For  $\lambda_D \ll R$  (no Debye layer overlap), PNP-NS predicts that the electroosmotic volumetric flow rate ( $Q_{eo}$ ) through a cylindrical channel of radius  $R$  and length  $L$  can be written as

$$Q_{eo} = \pi R^2 |v_{eo}|, \quad v_{eo} = \frac{\varepsilon_0 \varepsilon_L \zeta_w \Delta V}{\eta L}, \quad (5)$$

with  $\varepsilon_L$  and  $\eta$  relative permittivity and viscosity of the electrolyte solution;  $\zeta_w$  is the average surface electrokinetic potential [40] and  $v_{eo}$  is the Helmholtz-Smoluchowski electroosmotic velocity, *i.e.* the velocity of the plug flow obtained when  $\lambda_D \ll R$  [41]. In this framework, the net charge density  $\rho_{el}$  and, hence, the total charge  $q_N$  inside the nanopore are function of  $\zeta_w$

$$q_N = 2\pi L \int_0^R dr r \rho_{el}(r) \approx -2\pi L \varepsilon_0 \varepsilon_L \frac{R}{\lambda_D} \zeta_w, \quad (6)$$

where in the rightmost term we considered that for  $R \gg \lambda_D$  the charge in the pore can be approximated as the product of pore surface  $2\pi RL$  times the surface charge of a planar Debye layer  $\varepsilon_0 \varepsilon_L \zeta_w / \lambda_D$  [19]. Thus,  $\zeta_w$  is proportional to  $q_N$  and, for Eq. (3), to  $\Delta V$ . Combining Eqs.(6) and (3) we get

$$\zeta_w = \frac{\lambda_D C_s \Delta V}{R 2\pi \varepsilon_0 \varepsilon_L L}, \quad (7)$$

that, when introduced into Eq. (5), leads to the parabolic expression for the EOF velocity

$$v_{eo} = \frac{\lambda_D C_s}{2\pi \eta R L^2} \Delta V^2 =$$

$$= \frac{\varepsilon_0 \varepsilon_S}{2\eta} \frac{\lambda_D}{R} \frac{(L-h)^2 (L-4\lambda_d)}{\ln(1+\frac{s}{R}) L^4} \Delta V^2. \quad (8)$$

Equations (5-8) are strictly valid only for  $\lambda_D \ll R$  and therefore, in principle, accurate quantitative predictions cannot be expected. Nevertheless, for the pore in Fig. 1d-f ( $L = 30$  Å and  $R = 10$  Å) the model predictions are in very good agreement with MD data. The capacitance  $C_s$ , Eq. (2), well predicts the dependence of net pore charge  $q_N$  on  $\Delta V$ , dashed line in Fig. 3a. The MD selectivity  $\Delta J$ , computed from the ionic currents shown in Supplementary Fig. S10, is reported in Fig. 3b, confirming the selectivity switch predicted by Eq.(4) of our model. The higher MD values may be explained by the convective contribution to ion transport that is not included in Eq. (1). Indeed, since the EOF is directed as the dominant ionic flow, it always results in an increase of selectivity. Finally, Eq.(8) gives an excellent quantitative estimation of the average electroosmotic velocity,  $v_{eo} = Q_{eo}/\pi R^2$ , with  $Q_{eo}$  computed from MD simulations, Fig. 3c.

**Effect of geometric parameters.** To verify the robustness of the observed phenomenon and the accuracy of the proposed quantitative model, we performed a second set of MD simulations focusing on the role of geometrical parameters. Each set of simulations is performed at  $\Delta V = +0.75$  V, by varying one single geometrical parameter, while keeping fixed all the others. Results are reported in Fig. 3d-g, with a sketch of the geometry reported in the inset of Fig. 3e. The electroosmotic velocity  $|v_{eo}|$  is reported on the top panels, while the total accumulated charge inside the nanopore  $|q_N|$  is shown in the bottom ones. In all cases we observe induced charge accumulation inside the pore and a concomitant EOF. The general trends predicted by our model are in good agreement with the simulations. The quasi-1D capacitance model, Eq. (2), predicts the MD data within two error bars for almost all cases. The analytical  $v_{eo}$ , Eq. (8), better matches the MD data for longer pores ( $L > 30$  Å), while it slightly overestimates the flow rates for the shorter ones, see Fig. 3d. Anyhow, the model correctly indicates that the dependence on  $L$  is non monotonic; this is due to the competing effect between the driving electric field  $E_z = \Delta V/L$ , that decreases with  $L$ , and the induced capacitance  $C_s$ , Eq. (2), that increases with  $L$ . The induced charge effect and EOF increase with the cavity depth  $d = L - h$ , Fig. 3e, consistently with the increase of the voltage drop between the pore lumen and the deeper portion of the cavity, see the quasi-1D pore capacitance model in Supplementary Note S1, and the electric potential maps in Supplementary Fig. S11. The geometrically induced selectivity vanishes for  $d \rightarrow 0$ , as trivially expected since the system becomes symmetric. The MD data of Fig. 3e refer to a pore with  $L = 30$  and, as for Fig. 3d, are in quantitative agreement with the model. We also ran simulations for  $L = 18$ , at different thickness  $s$  and radius  $R$ . In both cases the model overestimates  $q_N$  and  $v_{eo}$  although capturing the trends of the

MD data, e.g., for increasing  $s$  the lateral capacitance decreases and so do  $q_N$  and  $v_{eo}$ . The apparent quantitative agreement for  $R < 10$  could be more probably ascribed to fortuitous compensation of different sources of atomistic effects, more than to a correct description of such extremely confined conditions.

The geometrically induced selectivity and the unidirectional EOF are not limited to nanometer and subnanometer scale. Eq. (8) allows to quantify EOF for pores of any size and can hence be employed for nanopore system design. As an example, in Supplementary Fig. S12, we report  $v_{eo}$  for a water electrolyte solution through a silicon nitride pore of radius of 20 nm. Such relatively large pores are widely used in experimental studies [42, 43] and the required surface patterning can be achieved with well established techniques [44]. Eq. (8) indicated that as the system size increases,  $|v_{eo}|$  decreases. This decrease can be partially compensated using materials with larger dielectric constant or increasing the Debye length, as both  $\lambda_D$  and  $\epsilon_S$  appear in the numerator of Eq. (8). The resulting EOF can be in principle experimentally tested. A possible technique is the one proposed by Secchi et al. [11] where the velocity field far from the pore is measured following the trajectory of tracers. This approach does not directly allow to measure the flow close to the pore but only at a distance of a few  $\mu\text{m}$ . In our system, a  $v_{eo} \simeq 0.1$  m/s at the exit of a pore of  $R = 20$  nm would result in a velocity of magnitude  $v \sim 10^{-4}$  m/s at a distance of 1  $\mu\text{m}$  from the pore (fluid velocity scales as  $1/r^2$ , where  $r$  is the distance from the pore). This value appears to be within the reach of the proposed experimental technique [11]. Another alternative is to infer the EOF from its effect on the capture of nanoparticles by a nanopore. Indeed, the capture rate is ruled by the competition/cooperation of different effects, the most relevant being electrophoresis, electroosmosis and dielectrophoresis [21–23]. Analytical expressions for the capture rate have been recently proposed [21] and, in principle, they allow to directly relate EOF and capture rate, if pore and particle geometry, charge and dielectric properties are known. Due to the difficulties in modelling pore entrance effects, quantitatively accurate estimations of EOF are not expected, nevertheless, a clear indication of the EOF direction and of the dependence of  $v_{eo}$  on  $\Delta V$  should be achievable.

**Effect of asymmetric electrolyte.** We performed a set of MD simulations of the solid system of Fig. 1d-f with a 2M KCl water solution to investigate the effect of an asymmetric electrolyte. The overall behavior of the system is similar to the symmetric electrolyte case. In particular, a selectivity switch and a unidirectional EOF are observed, see Fig. 4a-c. Some asymmetries are evident, as expected. At equilibrium,  $\Delta V = 0$ , the system exhibits an intrinsic net positive charge accumulation inside the nanopore lumen ( $q_N \simeq 0.2e$ , Fig. 4a,d), despite the zero surface charge of the solid. Indeed, the asymmetric electrolyte develops an equilibrium charge layering at

the solid-liquid interface, Fig. 4d. This is also evident from the peculiar orientation of the water molecules at the wall, forming surface dipoles, Fig. 4e. The presence of interfacial dipoles generate an intrinsic polarization of the membrane and, hence, a non-zero surface potential, Fig. 4f. The formation of a non-zero surface potential in uncharged nanopores due to electrolyte asymmetries was proposed by Dukhin et al. [46] and later investigated by other authors [47, 48]. For instance, in Kim et al. [47] it was shown that the different hydration forces among cations and anions lead to a slightly different equilibrium position of positive and negative charges (*i.e.* a charge layering) at the solid/liquid interface of uncharged hydrophobic nanopores. The charge layering results in a non-zero surface potential and EOF. A similar layering was also found in Mucha et al. [48] at liquid/air interfaces.

Hence, for an asymmetric electrolyte, two effects rule the pore charge accumulation, namely, the equilibrium surface potential of the pore lumen that leads to an intrinsic selectivity (cation, in the present case) and the induced charge mechanism due to the presence of the lateral cavity. We observe different behaviors under opposite  $\Delta V$ , see Fig. 4a-c. For  $\Delta V < 0$ , the charge inside the nanopore,  $q_N$ , remains fairly constant and the selectivity and EOF are both roughly proportional to  $\Delta V$ . For  $\Delta V > 0$ , instead,  $q_N$  decreases linearly with  $\Delta V$ , and, coherently to the induced charge mechanism, the selectivity and EOF are quadratic. In such a complex scenario, the theoretical expressions derived for the perfect symmetric case (dashed gray lines in Fig. 4a-c) fall short in predicting quantitatively the selectivity and EOF intensity. Nevertheless, they still provide the order of magnitude of the effect.

**A biological example: the CsgG nanopore.** We then verified if the geometrically induced selectivity switch and the unidirectional EOF occur for some biological nanopores. We selected as a possible candidate the curli specific gene G (CsgG) protein from *E. coli*. This pore is currently used in commercial devices for nanopore DNA sequencing [39, 49]. CsgG is a non-americ membrane protein, part of a transport machinery comprising at least seven proteins encoded by two operons [50] that excretes functional amyloids [51], the curli proteins [37, 38]. The CsgG pore is constituted by two large vestibules on the cis and trans side connected by a constriction of diameter  $\simeq 1.2$  nm, formed by the so-called C-loop, Fig. 5a.

CsgG pore lumen is irregular, yet the shape of its constriction region resembles the cylindrical pore surrounded by a coaxial cavity, albeit being more complex. For example, the constriction region is not straight but has a cleft at about one third of its length. The lateral cavity is formed between the transmembrane  $\beta$ -barrel and the C-loop (residues 47-58, see the inset of Fig. 5a) that is held in place by the cis mixed  $\alpha\beta$  domains. The geometry of the lateral cavity is wedged and inclined, with a

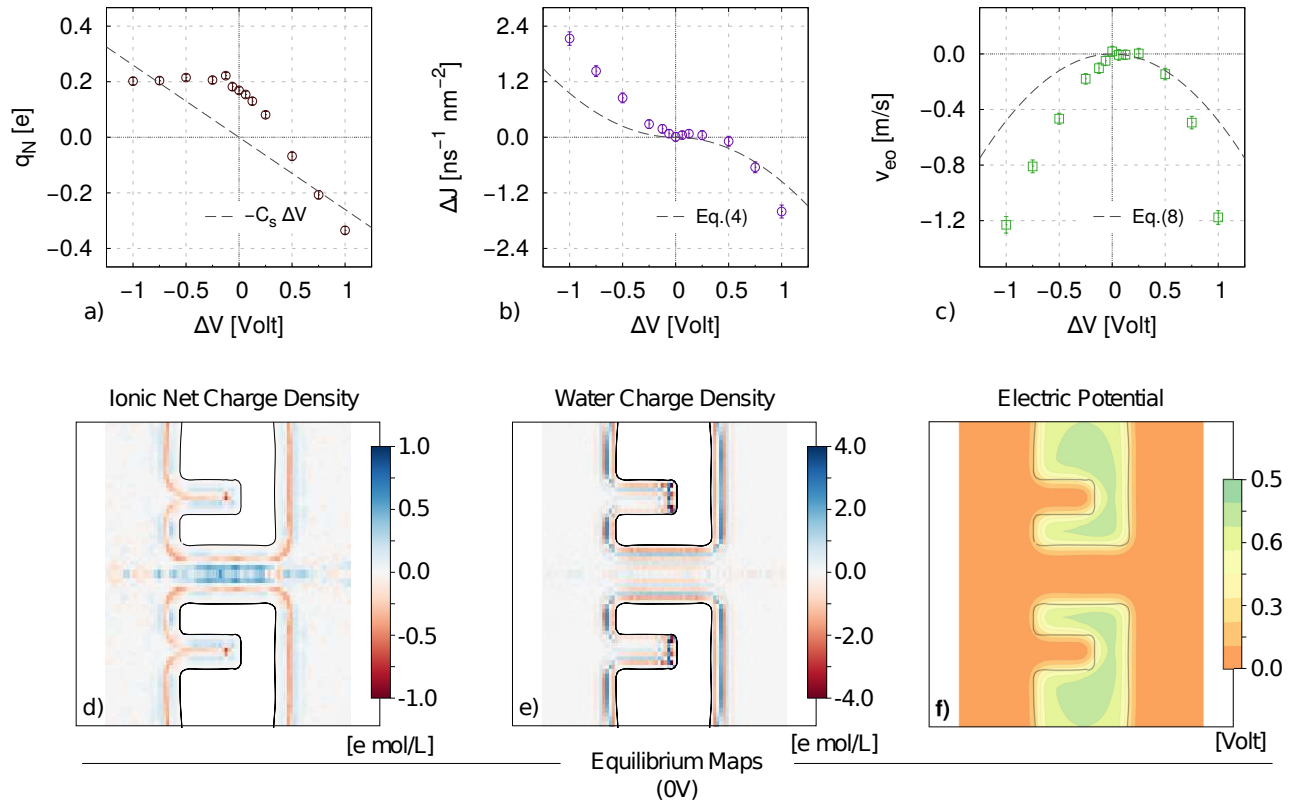
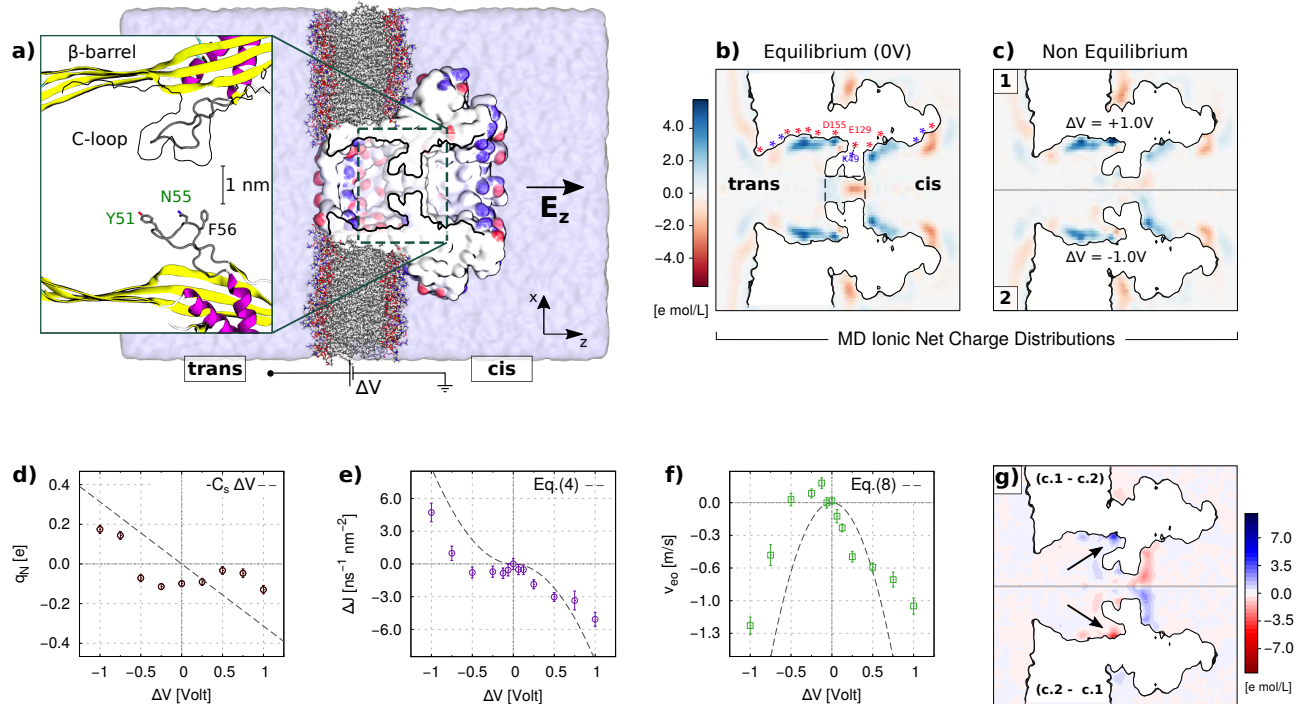


FIG. 4. **Effect of asymmetric electrolyte.** **a-c)** Charge in the pore  $q_N$ , selectivity  $\Delta J$ , and average EO velocity  $v_{eo}$  from MD simulation of a nanopore with  $R = 10\text{\AA}$ ,  $L = 30\text{\AA}$ ,  $h = 10\text{\AA}$ ,  $s = 9\text{\AA}$ ,  $w = 12\text{\AA}$  (same as Fig. 1d-f) in a 2M KCl water solution (symbols). Gray dashed lines represent the theoretical predictions for a symmetric case, *i.e.*  $q_N = C_s \Delta V$  for the nanopore charge and Eqs. (3-8) for  $\Delta J$ , and  $v_{eo}$ ; The other parameters used are  $\mu = 1.0 \times 10^{32}/(\text{V ns})$ ,  $\lambda_D = 2.1\text{\AA}$ ,  $\varepsilon_S = 1$ ;  $\eta = 0.3\text{ mPa s}$  (TIP3P viscosity  $\simeq 1/3$  experimental water [45]). **d-f)** Ionic and water charge density and electric potential at equilibrium ( $\Delta V = 0$ ), showing the intrinsic polarization and layering at the solid liquid interface, despite the zero charge of the solid membrane. The potential difference between the bulk liquid and the membrane interior is related to the presence of interfacial charge dipoles. MD distributions and fluxes are averaged over 800 ns MD trajectory (16 000 frames). Errors are calculated using a block average protocol with a block length of 10 ns.

moderately polar surface composition. D155 is the only exposed charged sidechain while K49 and E129 form a stable salt bridge and are only partially solvent accessible, Fig. 5b. Several surface charges are present in the lumen and are marked in Fig. 5b with blue and red asterisks. The  $\beta$ -barrel is overall negatively charged with four acidic residues and two basic ones for each of the nine protomers. The cis-vestibule has two acidic residues near the constriction. Other charged residues are located at the entrances of the cis and trans vestibules. Globally, the pore total charge is zero and the constriction has no charged residues exposed.

We performed a set of MD simulations at different applied voltages, in 2M KCl water solution. At equilibrium ( $\Delta V = 0$ ) the pore exhibits a net negative charge  $q_N$  in the constriction, Fig. 5b,d. For  $\Delta V > 0$ ,  $q_N$  remains quite constant and the anion selectivity ( $\Delta J < 0$ ) shows a linear scaling with  $\Delta V$ , Fig. 5e. EOF is negative, since the water flow follows the motion of the anions, Fig. 5f. For small negative  $\Delta V$ , the pore is still anion selective ( $q_N < 0$  and  $\Delta J < 0$ ) and  $v_{eo}$  becomes positive

since, again, the water flow follows the motion of the anions. This is the usual behavior of an electroosmotic flow where the charge accumulation in the pore is due to a wall potential independent of the  $\Delta V$ . An inversion of both the accumulated charge  $q_N$  and selectivity is observed for large negative voltages,  $\Delta V < -0.5\text{ V}$ , consistently with the geometrically induced selectivity switch mechanism. Gray dashed lines in Fig. 5d-f report the predictions of the theoretical model. For completeness, the current-voltage curve is reported in Supplementary Fig. S13. Although the pore geometry is quite far from the ideal model system of Fig. 1 and asymmetries are present in the curves, the simplified model is still able to capture the order of magnitude of the EOF. As in the solid state nanopore with asymmetric electrolyte discussed in Fig. 4, the data suggest that the presence of an equilibrium (intrinsic) net charge in the pore results in a sort of shift of the EOF curve with respect to the theoretical parabolic prediction. In the solid-state case of Fig. 4, the pore is intrinsically cation selective (at low  $\Delta V$ ) and the selectivity inversion occurs at a positive  $\Delta V$ . Accord-



**FIG. 5. The CsgG biological nanopore in 2M KCl water solution.** **a)** MD set-up. A volume rendering representation of the cross-section of the pore (white) embedded in a lipid membrane, with exposed charged residues colored (blue positive, red negative). Water and ions are omitted for clarity. The inset shows a zoom of the pore constriction with the cartoon representation of secondary structure on the top side, and licorice representation of the residues forming the constriction surface Y51, N55 (hydrophilic, green labels) and F56 (hydrophobic, black label) on the bottom. **b)** Equilibrium ( $\Delta V = 0$  V) and **c)** non-equilibrium ( $\Delta V = \pm 1$  V) MD ionic net charge density distributions. The asterisks in **b)** indicate the charged residues exposed toward the nanopore lumen. **d)** Charge in the constriction, **e)** selectivity and **f)** electroosmotic velocity as functions of the applied voltage  $\Delta V$ . Dashed lines represent the theoretical prediction ( $L = 18$  Å,  $R = 6$  Å,  $s = 9$  Å,  $h = 5$  Å and  $\epsilon_S = 6$ ); The other parameters for the solvent are the same used in Fig. 4. **g)** Difference of the panels **c.1** and **c.2**, pointing out the opposite charge accumulation inside the lateral cavity at opposite voltages  $\Delta V = \pm 1$  V. In panels **a-c** and **g** the black line delimiting the pore and the membrane is the water density contour level  $\rho = 0.5 \rho_{bulk}$ , with  $\rho_{bulk}$  the bulk water density. Fluxes and maps are obtained from 280 ns MD production runs. All the trajectories are sampled each 20 ps and analyzed discarding the first 10 ns. Errors are calculated using a block average protocol with a block length of 10 ns.

ingly, the maximum of EOF is shifted towards positive  $\Delta V$ . Conversely, in CsgG, the pore is intrinsically anion selective (at low  $\Delta V$ ) so the selectivity inversion occurs at a negative  $\Delta V$  and the EOF curve is shifted towards the left.

Further details on the charge distributions for  $\Delta V = 0$  are reported in Fig. 5b. The map shows several charge accumulation spots due to the solvent-exposed charged residues in the two vestibules. Another relevant difference with respect to the ideal solid-state case is the charge distribution in the constriction at equilibrium ( $\Delta V = 0$ ), that shows a relative accumulation of positive (negative) ions on the trans (cis) side of the constriction. This peculiar distribution and the consequent intrinsic anion selectivity may reflect the complex shape of the constriction and the different hydrophathy of the surface, composed by hydrophilic (Y51 and N55) and hydropho-

bic (F56) parts, see the inset in Fig. 5a. Nevertheless, in agreement with our induced charge model, when an external  $\Delta V$  is applied, ions accumulate in the lateral cavity of CsgG (altering also the charge distribution in the constriction), as shown in Fig. 5c. This voltage dependent behavior is better highlighted by Fig. 5g, representing the difference of the maps at  $\Delta V = 1$  V and  $\Delta V = -1$  V. An alternative representation of the differential maps with respect to the equilibrium (0V, Fig. 5b) is reported in Supplementary Fig. S13. For comparison, we also ran simulations for a neutralized pore. Charge accumulation spots in the pore vestibules are much less evident, nevertheless the charge distribution in the constriction is quite similar to the unmodified CgsG and consequently, ion currents, selectivity and EOF are, in essence, unchanged, see Supplementary Fig. S14. In addition, in Supplementary Fig. S15 we also reported an

analysis that attempts to compare the induced charge EOF predicted by our geometrical model (that scales as  $\Delta V^2$ ) and the expected linear EOF due to intrinsic anion selectivity at different voltages. This analysis indicates that for  $|\Delta V| \lesssim 0.3$  V the dominant contribution is the intrinsic selectivity while for  $|\Delta V| \gtrsim 0.3$  V, induced charge mechanism dominates the EOF. MD data for negative  $\Delta V$ , where selectivity inversion is observed, approximatively supports this theoretical threshold.

## II. CONCLUSION

We presented a mechanism of geometrically induced selectivity that switches with the applied voltage polarity in uncharged cylindrical nanopores, giving rise to unidirectional electroosmotic flow. We derived an analytical model and we tested our predictions against Molecular Dynamics simulations. The phenomenon is robust under variation of the system geometry (e.g., cavity size, pore length) and our model provides a quantitatively accurate estimation of the electroosmotic velocity that can be used for nanopore system design. Unidirectional electroosmotic flow occurs also for a biological pore, the CsgG protein, whose shape resembles the cavity-nanopore ideal system. A similar pore structure is found also in other secretion related proteins of known structure such as InvG [52] and PilQ [53] secretins, extending the possibility to use biomolecular scaffolds to achieve geometrically induced selectivity. Moreover, the surface patterning needed to elicit this effect is achievable by modern nanofabrication technology, such as electron-beam decoration of graphene [54], focused ion beam [55], or electron beam lithography, reactive ion etching of TEM-drilled silicon nitride membranes [44]. The mechanism we unraveled allows to induce an ion selectivity without altering the pore shape, surface charge or chemistry and, consequently, it can open the way to more flexible design of selective membranes. The magnitude of the EOF associated to geometrically induced selectivity is comparable to other more common sources of EOF such as fixed surface charges [20, 22, 23, 56, 57]. Consequently, we expect that such a mechanism may find application in all the nanopore technologies where EOF is already used. One example is alternate current electroosmotic pumps [36, 58]. The average EOF intensity for a membrane constituted by conical nanopores [58] is of the same order of the one we observed. Similarly, our mechanism may be employed in nanopore-based single molecule sensing devices, where calibrating the competition/cooperation between electroosmosis and electrophoresis [20, 21] is crucial to control particle capture, especially for neutral or weakly charged molecules such as proteins and peptides [22, 23]. Since the EOF is induced without modification of the pore interior, in principle the geometric mechanism we propose to generate selectivity and electroosmotic flow may allow to separately and inde-

pendently engineer the pore lumen to improve the sensing performance and the external cavity to control EOF.

## III. METHODS

**General Molecular Dynamics Simulations Methods.** All MD runs were carried out using NAMD [59], using a time-step of  $\Delta t = 2.0$  fs and Particle Mesh Ewald [60] method with 1.0 spaced grid for long range electrostatic interactions. A cutoff of 12 with switching distance of 14 was set for the short range non-bonded interactions. Periodic boundary conditions with hexagonal prism cell is used unless otherwise stated. Langevin thermostat was used for all the simulations. Nosé-Hoover Langevin piston pressure control was used for constant pressure simulations [61].

**Solid-state pore set-up.** Our model system, represented in Fig. 1d, is composed by a hexagonal solid membrane of thickness  $L$  with a cylindrical nanopore of radius  $R$ , surrounded by a coaxial cavity of width  $w$  and height  $d = L - h$ , at a distance  $s$  from the nanopore wall. The hexagon apothem  $a_h$ , (see the top-view inset of the membrane in Fig. 1d, green line) is  $a_h = 2.1(R + s + w)$ . The membrane is composed of hexagonally packed uncharged atoms, see Supplementary Fig. S4. For Figs. (1-3), the membrane is immersed into a 2M electrolyte solution, composed of a symmetrical polar fluid (see below) in which oppositely charged ions are dissolved. For Fig. 4, the membrane is immersed into a 2M KCl water solution, using standard CHARMM parameters for TIP3P water molecules and potassium ( $K^+$ ) and chloride ( $Cl^-$ ) ions. The  $z$ -dimension of each simulation cell is about  $H_z = 2a_h + L$ , with  $L$  height of the membrane, to ensure that the liquid height surrounding the pore entrance is greater than two times the pore diameter. The system is equilibrated with a constant pressure (flexible cell NPT) run at  $P = 1$  atm and  $T = 250$  K, keeping the x,y plane area fixed. The production runs are conducted at constant volume, temperature and particle number (NVT ensemble), with a constant and homogeneous electric field  $\mathbf{E} = (0, 0, E_z)$  applied to charged atoms.

**Model Dipolar Fluid.** The model fluid is composed of diatomic molecules, each formed by two atoms of mass  $m = 10$  Da, of opposite charge  $q^+ = 0.5e$  and  $q^- = -0.5e$ , covalently bound through a harmonic potential  $U = k_b(r - r_0)^2$  where  $r$  is the distance between the two atoms,  $r_0 = 1$  the equilibrium distance and  $k_b = 450$  kcal/(mol<sup>2</sup>) the spring constant, see Supplementary Fig. S4. Intramolecular interactions are modeled via a standard Coulomb potential plus a Lennard-Jones (LJ) potential, with  $\epsilon_{LL} = 0.1$  kcal/mol and  $\sigma_{LL} = 2.68$ . The above parameters were chosen to have volume, dipole moment and mass similar to those of TIP3P water [62]. The fluid exhibits a stable liquid phase in the temperature range  $200 \leq T \leq 400$  K, under a pressure of  $P = 1$  atm, see the phase diagram

in Supplementary Fig. S5. At  $T = 250$  K, the liquid density is  $\rho = 55.5$  mol/L while the relative electric permittivity is  $\epsilon_L = 83.2 \pm 4.6$  and dynamic viscosity  $\eta = 0.35 \pm 0.02$  mPas. Relative permittivity  $\epsilon_L$  was assessed by computing the dipole moment fluctuations in equilibrium NVT MD simulations [63]; non-equilibrium estimation lead to similar results, Supplementary Fig. S6. Viscosity  $\eta$  was estimated by applying a shear stress on the top of a liquid volume and measuring the slope of the resulting velocity profile (Couette flow), Supplementary Fig. S7.

Non-bonded interactions between fluid and solid molecules were modelled using a LJ potential, with  $\epsilon_{SL} = 0.8\epsilon_{LL}$  and  $\sigma_{SL} = \sigma_{LL}$  (SL, solid-liquid), resulting in a hydrophilic pore. The wettability of the solid was assessed by evaluating the contact angle  $\theta$  of a cylindrical drop of fluid onto the surface as a function of temperature and liquid-solid interaction potential  $\epsilon_{SL}$  [64], see Supplementary Fig. S8. For the selected  $\epsilon_{SL}/\epsilon_{LL}$  ratio, the contact angle is  $\theta \simeq 60^\circ$ .

The dissolved ions are composed by monovalent charged particles with charges  $q^\pm = \pm 1e$  and mass 40 Da. Non-bonded interactions of each ion with other atoms are described in Supplementary Fig. S4. Ion diffusion coefficient for a 2M solution at  $P = 1$  atm and  $T = 250$  K, is  $D = 94.4 \pm 0.7$   $^2$ /ns, corresponding to an ion mobility  $\mu = 4.4 \times 10^3$   $^2$ /(V ns); the diffusion coefficient  $D$  is estimated from the mean squared displacement (MSD), see Supplementary Fig. S9.

**CsgG pore set-up.** The membrane-CsgG system was assembled using a protocol similar to the one reported in [65, 66]. The system was built starting from the CsgG x-ray crystal structure taken from the Protein Data Bank, PDB ID: 4UV3 [38] downloaded from the OPM database [67]. The beta-barrel missing fragments (F144, F193 to L199) are modeled by using SWISS-MODEL server [68]. Other missing fragments (V258 to S262), located in the periphery of the cis side of the pore, were deemed to be not important for the ion and EOF transport and were not taken into account. The POPC lipid membrane, the water molecules, and the ions to neutralize the system were added using VMD [69]. Salt concentration was set to 2M KCl. The CHARMM36 force field [70] was employed to model lipid, protein, and TIP3P water molecules [62]. Non-bonded fix corrections were applied for ions [71]. All covalent bonds with hydrogen were kept rigid, using SETTLE [72] for water molecules and SHAKE/RATTLE [73] for the rest of the system.

The energy of the system was first minimized for 10 000 steps using the conjugate gradient method. Then a pre-equilibration of 1 ns is performed to let the lipid tails melt and the electrolyte relax: the temperature was increased from 0 to 300 K in 100 ps, and then the Langevin thermostat with a damping coefficient of 1  $\text{ps}^{-1}$  was applied to all non-hydrogen atoms; external forces were applied to the water molecules to avoid their penetration into the membrane, while the back-

bone of the protein and the lipid heads were constrained to their initial positions by means of harmonic springs,  $k_b = 1$  kcal/(mol $^2$ ); Nose-Hoover Langevin method, with period 100 fs and decay of 50 fs, was used to keep a pressure of 1 atm, allowing the unit cell volume to fluctuate, by keeping the ratio between the x,y axis constant. A second equilibration run of 1.3 ns was performed to compact the membrane, letting the lipid heads unconstrained, and reducing the spring constant on the protein backbone to  $k_b = 0.5$  kcal/(mol $^2$ ), until the three unit cell vectors reach a stationary value. The last equilibration step consisted of a 3 ns NPT run (as the previous step, keeping the ratio between the x,y axis constant) where all the atoms were unconstrained and no external forces applied to the water molecules. At the end of the equilibration procedure, the hexagonal periodic box has the following basis vectors:  $v_x = (179, 0, 0)$ ,  $v_y = (89, 155, 0)$ , and  $v_z = (243, 0, 0)$ , for a total of 680 827 atoms.

**Current measurements.** The production runs were performed at constant volume, temperature and particle number (NVT ensemble). The length of each simulation is indicated in the caption of the figures. For each case, a uniform and constant external electric field  $\mathbf{E} = (0, 0, E_z)$  was applied perpendicularly to the membrane. This protocol was shown to be equivalent to the application of a constant voltage  $\Delta V = E_z L_z$  [74], ( $E_z > 0$  for  $\Delta V > 0$ , as indicated in Fig. 1b). In the solid-state nanopores, the solid atoms are constrained to initial lattice positions with a harmonic spring,  $k_b = 100$  kcal/(mol $^2$ ), the solid membrane is thermostated and coordinates are saved every  $\Delta t = 50$  ps. In the CsgG case, lipid head phosphorus are harmonically constrained to the position of the last configuration of the equilibration phase, with  $k_b = 10$  kcal/(mol $^2$ ), and a thermostat is applied to the lipid and protein atoms (not hydrogens). Snapshots are saved every  $\Delta t = 40$  ps. The average current in the interval  $[t, t + \Delta t]$  is estimated as [65, 66, 75]

$$I(t) = \frac{1}{\Delta t L_z} \sum_{i=1}^N q_i [z_i(t + \Delta t) - z_i(t)] \quad (9)$$

where  $q_i$  and  $z_i$  are the charge and the z-coordinate of the  $i$ -th atom, respectively. Ionic currents (either  $\text{K}^+$  and  $\text{Cl}^-$  or model ions) were computed by restricting the sum over the atoms of corresponding type [65]. The mean current is obtained via a block average of  $I(t)$  (each block corresponding to 10 ns) after discarding a transient of 30 ns. The EOF is measured in a similar way, computing the summation over the fluid atoms and using the mass instead of the charge in Eq. (9). The results are then converted from mass flow rate to volumetric flow rate using the bulk liquid density.

**Charge density, velocity fields and potential maps.** Using the VMD *Volmap* plug-in [69], we divided the system in cubic cells of size  $\Delta x = \Delta y = \Delta z = 1$   $\text{\AA}$ , and we calculated the average charge in each cell using the frames of the stationary state of the production run. A similar protocol is applied for the velocity profiles. In a

given frame  $f$ , the velocity of the  $i$ -th atom is computed as  $\mathbf{v}_i(f) = (\mathbf{x}_i(f+1) - \mathbf{x}_i(f-1))/(2\Delta t)$ , with  $\mathbf{x}_i(f)$  its position and  $\Delta t$  the sampling interval. The average velocity in each cell is then calculated averaging over the particles belonging to the cell and over time. The electric potential maps are computed by using the *pmepot* plug-in of VMD [65] based on the particle-mesh Ewald method (PME). We then transformed the charge density and the velocity fields from the  $(x, y, z)$  Cartesian coordinate system to a cylindrical coordinate system  $(r, z, \alpha)$  and performed a further averaging on  $\alpha$  to get density and velocity fields in the  $(r, z)$  plane as the ones showed in Fig. 1e-f and Fig. 5b-c. Confidence intervals in Fig. 1e were obtained using a block average with each block corresponding to 10 ns.

**Supplementary Information.** Details for the calculation of Induced Debye layer capacitance for the cavity-nanopore system. PNP-NS model for EOF and

comments on the model assumptions. Characterization of our atomistic model for symmetric electrolyte solution in terms of phase diagram, relative electrical permittivity, wetting, ion mobility and viscosity. Ion currents as a function of the voltage for our model system and for the CsgG nanopore. Electric potential for different cavity sizes. EOF prediction for a neutral Silicon Nitride nanopore of radius 20 nm. Alternative maps of Fig. 5g. Fluxes and charge density maps for Neutral Model of CsgG nanopore. Comparison between parabolic induced charge and linear fixed charge EOF.

**Acknowledgements** The authors acknowledge supercomputer time provided through HP10BGBB69 Iskra B Grant by CINECA and s958 Production Grants by CSCS.

**Competing interest** The authors declare no competing interests.

- 
- [1] Bocquet, L. Nanofluidics coming of age. *Nature Materials* **2020**, *19*, 254–256.
- [2] Hong, S.; Constans, C.; Surmani Martins, M. V.; Seow, Y. C.; Guevara Carrio, J. A.; Garaj, S. Scalable graphene-based membranes for ionic sieving with ultra-high charge selectivity. *Nano letters* **2017**, *17*, 728–732.
- [3] Siwy, Z. S. Ion-current rectification in nanopores and nanotubes with broken symmetry. *Advanced Functional Materials* **2006**, *16*, 735–746.
- [4] Karnik, R.; Duan, C.; Castelino, K.; Daiguji, H.; Majumdar, A. Rectification of ionic current in a nanofluidic diode. *Nano letters* **2007**, *7*, 547–551.
- [5] Beckstein, O.; Biggin, P. C.; Sansom, M. S. A hydrophobic gating mechanism for nanopores. *The Journal of Physical Chemistry B* **2001**, *105*, 12902–12905.
- [6] Powell, M. R.; Cleary, L.; Davenport, M.; Shea, K. J.; Siwy, Z. S. Electric-field-induced wetting and dewetting in single hydrophobic nanopores. *Nature nanotechnology* **2011**, *6*, 798–802.
- [7] Wilson, J.; Aksimentiev, A. Water-compression gating of nanopore transport. *Physical review letters* **2018**, *120*, 268101.
- [8] Camisasca, G.; Tinti, A.; Giacomello, A. Gas-Induced Drying of Nanopores. *The Journal of Physical Chemistry Letters* **2020**, *11*, 9171–9177.
- [9] Agre, P. Aquaporin water channels (Nobel lecture). *Angewandte Chemie International Edition* **2004**, *43*, 4278–4290.
- [10] Gravelle, S.; Joly, L.; Ybert, C.; Bocquet, L. Large permeabilities of hourglass nanopores: From hydrodynamics to single file transport. *The Journal of chemical physics* **2014**, *141*, 18C526.
- [11] Secchi, E.; Marbach, S.; Niguès, A.; Stein, D.; Siria, A.; Bocquet, L. Massive radius-dependent flow slippage in carbon nanotubes. *Nature* **2016**, *537*, 210–213.
- [12] Holt, J. K.; Park, H. G.; Wang, Y.; Stadermann, M.; Artyukhin, A. B.; Grigoropoulos, C. P.; Noy, A.; Bakkajin, O. Fast mass transport through sub-2-nanometer carbon nanotubes. *Science* **2006**, *312*, 1034–1037.
- [13] Kavokine, N.; Netz, R. R.; Bocquet, L. Fluids at the Nanoscale: From Continuum to Subcontinuum Transport. *Annual Review of Fluid Mechanics* **2020**, *53*.
- [14] Bétermier, F.; Cressiot, B.; Di Muccio, G.; Jarroux, N.; Bacri, L.; Della Rocca, B. M.; Chinappi, M.; Pelta, J.; Tarascon, J.-M. Single-sulfur atom discrimination of polysulfides with a protein nanopore for improved batteries. *Communications Materials* **2020**, *1*, 1–11.
- [15] Gu, L.-Q.; Braha, O.; Conlan, S.; Cheley, S.; Bayley, H. Stochastic sensing of organic analytes by a pore-forming protein containing a molecular adapter. *Nature* **1999**, *398*, 686–690.
- [16] Feng, J.; Graf, M.; Liu, K.; Ovchinnikov, D.; Dumcenco, D.; Heiranian, M.; Nandigana, V.; Aluru, N. R.; Kis, A.; Radenovic, A. Single-layer MoS<sub>2</sub> nanopores as nanopower generators. *Nature* **2016**, *536*, 197–200.
- [17] Siria, A.; Poncharal, P.; Bianco, A.-L.; Fulcrand, R.; Blase, X.; Purcell, S. T.; Bocquet, L. Giant osmotic energy conversion measured in a single transmembrane boron nitride nanotube. *Nature* **2013**, *494*, 455–458.
- [18] Tu, Y.-M.; Song, W.; Ren, T.; Shen, Y.-x.; Chowdhury, R.; Rajapaksha, P.; Culp, T. E.; Samineni, L.; Lang, C.; Thokkadam, A. et al. Rapid fabrication of precise high-throughput filters from membrane protein nanosheets. *Nature Materials* **2020**, *19*, 347–354.
- [19] Schoch, R. B.; Han, J.; Renaud, P. Transport phenomena in nanofluidics. *Reviews of modern physics* **2008**, *80*, 839.
- [20] Boukhet, M.; Piguet, F.; Ouldali, H.; Pastoriza-Gallego, M.; Pelta, J.; Oukhaled, A. Probing driving forces in aerolysin and  $\alpha$ -hemolysin biological nanopores: electrophoresis versus electroosmosis. *Nanoscale* **2016**, *8*, 18352–18359.
- [21] Chinappi, M.; Yamaji, M.; Kawano, R.; Cecconi, F. Analytical Model for Particle Capture in Nanopores Elucidates Competition among Electrophoresis, Electroosmo-

- sis, and Dielectrophoresis. *ACS nano* **2020**, *14*, 15816–15828.
- [22] Huang, G.; Willems, K.; Soskine, M.; Wloka, C.; Maglia, G. Electro-osmotic capture and ionic discrimination of peptide and protein biomarkers with FraC nanopores. *Nature communications* **2017**, *8*, 1–11.
- [23] Asandei, A.; Schiopu, I.; Chinappi, M.; Seo, C. H.; Park, Y.; Luchian, T. Electroosmotic trap against the electrophoretic force near a protein nanopore reveals peptide dynamics during capture and translocation. *ACS applied materials & interfaces* **2016**, *8*, 13166–13179.
- [24] Ramírez, P.; Mafe, S.; Alcaraz, A.; Cervera, J. Modeling of pH-switchable ion transport and selectivity in nanopore membranes with fixed charges. *The Journal of Physical Chemistry B* **2003**, *107*, 13178–13187.
- [25] Small, L. J.; Wheeler, D. R.; Spoerke, E. D. Nanoporous membranes with electrochemically switchable, chemically stabilized ionic selectivity. *Nanoscale* **2015**, *7*, 16909–16920.
- [26] Zeng, Z.; Yeh, L.-H.; Zhang, M.; Qian, S. Ion transport and selectivity in biomimetic nanopores with pH-tunable zwitterionic polyelectrolyte brushes. *Nanoscale* **2015**, *7*, 17020–17029.
- [27] Nishizawa, M.; Menon, V. P.; Martin, C. R. Metal nanotubule membranes with electrochemically switchable ion-transport selectivity. *Science* **1995**, *268*, 700–702.
- [28] Kalman, E. B.; Sudre, O.; Vlassioux, I.; Siwy, Z. S. Control of ionic transport through gated single conical nanopores. *Analytical and bioanalytical chemistry* **2009**, *394*, 413–419.
- [29] Guan, W.; Li, S. X.; Reed, M. A. Voltage gated ion and molecule transport in engineered nanochannels: theory, fabrication and applications. *Nanotechnology* **2014**, *25*, 122001.
- [30] Cheng, C.; Jiang, G.; Simon, G. P.; Liu, J. Z.; Li, D. Low-voltage electrostatic modulation of ion diffusion through layered graphene-based nanoporous membranes. *Nature nanotechnology* **2018**, *13*, 685–690.
- [31] Fuest, M.; Boone, C.; Rangharajan, K. K.; Conlisk, A. T.; Prakash, S. A three-state nanofluidic field effect switch. *Nano letters* **2015**, *15*, 2365–2371.
- [32] Ren, R.; Zhang, Y.; Nadappuram, B. P.; Akpınar, B.; Klenerman, D.; Ivanov, A. P.; Edel, J. B.; Korchev, Y. Nanopore extended field-effect transistor for selective single-molecule biosensing. *Nature communications* **2017**, *8*, 1–9.
- [33] Bazant, M. Z.; Squires, T. M. Induced-charge electrokinetic phenomena. *Current Opinion in Colloid & Interface Science* **2010**, *15*, 203–213.
- [34] Ajdari, A. Pumping liquids using asymmetric electrode arrays. *Physical Review E* **2000**, *61*, R45.
- [35] Yao, Y.; Wen, C.; Pham, N. H.; Zhang, S.-L. On induced surface charge in solid-state nanopores. *Langmuir* **2020**, *36*, 8874–8882.
- [36] Hsu, W.-L.; Hwang, J.; Daiguji, H. Theory of Transport-Induced-Charge Electroosmotic Pumping toward Alternating Current Resistive Pulse Sensing. *ACS sensors* **2018**, *3*, 2320–2326.
- [37] Cao, B.; Zhao, Y.; Kou, Y.; Ni, D.; Zhang, X. C.; Huang, Y. Structure of the nonameric bacterial amyloid secretion channel. *Proceedings of the National Academy of Sciences* **2014**, *111*, E5439–E5444.
- [38] Goyal, P.; Krasteva, P. V.; Van Gerven, N.; Gubellini, F.; Van den Broeck, I.; Troupiotis-Tsailaki, A.; Jonckheere, W.; Péhau-Arnaudet, G.; Pinkner, J. S.; Chapman, M. R. et al. Structural and mechanistic insights into the bacterial amyloid secretion channel CsgG. *Nature* **2014**, *516*, 250.
- [39] Van der Verren, S. E.; Van Gerven, N.; Jonckheere, W.; Hambley, R.; Singh, P.; Kilgour, J.; Jordan, M.; Wallace, E. J.; Jayasinghe, L.; Remaut, H. A dual-constriction biological nanopore resolves homonucleotide sequences with high fidelity. *Nature biotechnology* **2020**, *38*, 1415–1420.
- [40] Herr, A.; Molho, J.; Santiago, J.; Mungal, M.; Kenny, T.; Garguilo, M. Electroosmotic capillary flow with nonuniform zeta potential. *Analytical chemistry* **2000**, *72*, 1053–1057.
- [41] Bruus, H. Theoretical microfluidics. 2008.
- [42] Zeng, S.; Wen, C.; Solomon, P.; Zhang, S.-L.; Zhang, Z. Rectification of protein translocation in truncated pyramidal nanopores. *Nature nanotechnology* **2019**, *14*, 1056–1062.
- [43] Houghtaling, J.; Ying, C.; Eggenberger, O. M.; Fennouri, A.; Nandivada, S.; Acharjee, M.; Li, J.; Hall, A. R.; Mayer, M. Estimation of shape, volume, and dipole moment of individual proteins freely transiting a synthetic nanopore. *ACS nano* **2019**, *13*, 5231–5242.
- [44] Chou, Y.-C.; Masih Das, P.; Monos, D. S.; Drndić, M. Lifetime and stability of silicon nitride nanopores and nanopore arrays for ionic measurements. *ACS nano* **2020**, *14*, 6715–6728.
- [45] Yeh, I.-C.; Hummer, G. System-size dependence of diffusion coefficients and viscosities from molecular dynamics simulations with periodic boundary conditions. *The Journal of Physical Chemistry B* **2004**, *108*, 15873–15879.
- [46] Dukhin, A.; Dukhin, S.; Goetz, P. Electrokinetics at high ionic strength and hypothesis of the double layer with zero surface charge. *Langmuir* **2005**, *21*, 9990–9997.
- [47] Kim, D.; Darve, E. High-ionic-strength electroosmotic flows in uncharged hydrophobic nanochannels. *Journal of colloid and interface science* **2009**, *330*, 194–200.
- [48] Mucha, M.; Frigato, T.; Levering, L. M.; Allen, H. C.; Tobias, D. J.; Dang, L. X.; Jungwirth, P. Unified Molecular Picture of the Surfaces of Aqueous Acid, Base, and Salt Solutions. *J. Phys. Chem. B* **2005**, *109*, 7617–7623.
- [49] Brown, C. G.; Clarke, J. Nanopore development at Oxford nanopore. *Nature biotechnology* **2016**, *34*, 810–811.
- [50] Chapman, M. R.; Robinson, L. S.; Pinkner, J. S.; Roth, R.; Heuser, J.; Hammar, M.; Normark, S.; Hultgren, S. J. Role of Escherichia coli Curli Operons in Directing Amyloid Fiber Formation. *Science* **2002**, *295*, 851–855.
- [51] Van Gerven, N.; Klein, R. D.; Hultgren, S. J.; Remaut, H. Bacterial Amyloid Formation: Structural Insights into Curli Biogenesis. *Trends in Microbiology* **2015**, *23*, 693–706.
- [52] Worrall, L.; Hong, C.; Vuckovic, M.; Deng, W.; Bergeron, J.; Majewski, D.; Huang, R.; Spreter, T.; Finlay, B.; Yu, Z. et al. Near-atomic-resolution cryo-EM analysis of the Salmonella T3S injectisome basal body. *Nature* **2016**, *540*, 597–601.
- [53] Weaver, S. J.; Ortega, D. R.; Sazinsky, M. H.; Dalia, T. N.; Dalia, A. B.; Jensen, G. J. CryoEM structure of the type IVa pilus secretin required for natural competence in *Vibrio cholerae*. *Nature communications* **2020**, *11*, 1–13.

- [54] Jin, Z.; Sun, W.; Ke, Y.; Shih, C.-J.; Paulus, G. L.; Wang, Q. H.; Mu, B.; Yin, P.; Strano, M. S. Metallized DNA nanolithography for encoding and transferring spatial information for graphene patterning. *Nature communications* **2013**, *4*, 1–9.
- [55] Semple, M.; Hryciw, A. C.; Li, P.; Flaim, E.; Iyer, A. K. Patterning of Complex, Nanometer-Scale Features in Wide-Area Gold Nanoplasmonic Structures Using Helium Focused Ion Beam Milling. *ACS Applied Materials & Interfaces* **2021**,
- [56] Willems, K.; Ruić, D.; Lucas, F. L.; Barman, U.; Verellen, N.; Hofkens, J.; Maglia, G.; Van Dorpe, P. Accurate modeling of a biological nanopore with an extended continuum framework. *Nanoscale* **2020**, *12*, 16775–16795.
- [57] Huang, G.; Willems, K.; Bartelds, M.; van Dorpe, P.; Soskine, M.; Maglia, G. Electro-osmotic vortices promote the capture of folded proteins by PlyAB nanopores. *Nano letters* **2020**, *20*, 3819–3827.
- [58] Wu, X.; Ramiah Rajasekaran, P.; Martin, C. R. An alternating current electroosmotic pump based on conical nanopore membranes. *Acs Nano* **2016**, *10*, 4637–4643.
- [59] Phillips, J. C.; Braun, R.; Wang, W.; Gumbart, J.; Tajkhorshid, E.; Villa, E.; Chipot, C.; Skeel, R. D.; Kale, L.; Schulten, K. Scalable molecular dynamics with NAMD. *Journal of computational chemistry* **2005**, *26*, 1781–1802.
- [60] Essmann, U.; Perera, L.; Berkowitz, M. L.; Darden, T.; Lee, H.; Pedersen, L. G. A smooth particle mesh Ewald method. *The Journal of chemical physics* **1995**, *103*, 8577–8593.
- [61] Martyna, G. J.; Tobias, D. J.; Klein, M. L. Constant pressure molecular dynamics algorithms. *The Journal of chemical physics* **1994**, *101*, 4177–4189.
- [62] Jorgensen, W. L.; Chandrasekhar, J.; Madura, J. D.; Impey, R. W.; Klein, M. L. Comparison of simple potential functions for simulating liquid water. *The Journal of chemical physics* **1983**, *79*, 926–935.
- [63] Raabe, G.; Sadus, R. J. Molecular dynamics simulation of the dielectric constant of water: The effect of bond flexibility. *The Journal of chemical physics* **2011**, *134*, 234501.
- [64] Weijs, J. H.; Marchand, A.; Andreotti, B.; Lohse, D.; Snoeijer, J. H. Origin of line tension for a Lennard-Jones nanodroplet. *Physics of fluids* **2011**, *23*, 022001.
- [65] Aksimentiev, A.; Schulten, K. Imaging  $\alpha$ -hemolysin with molecular dynamics: ionic conductance, osmotic permeability, and the electrostatic potential map. *Biophysical journal* **2005**, *88*, 3745–3761.
- [66] Bonome, E. L.; Cecconi, F.; Chinappi, M. Electroosmotic flow through an  $\alpha$ -hemolysin nanopore. *Microfluidics and Nanofluidics* **2017**, *21*, 96.
- [67] Lomize, M. A.; Lomize, A. L.; Pogozheva, I. D.; Mosberg, H. I. OPM: orientations of proteins in membranes database. *Bioinformatics* **2006**, *22*, 623–625.
- [68] Schwede, T.; Kopp, J.; Guex, N.; Peitsch, M. C. SWISS-MODEL: an automated protein homology-modeling server. *Nucleic acids research* **2003**, *31*, 3381–3385.
- [69] Humphrey, W.; Dalke, A.; Schulten, K. VMD: visual molecular dynamics. *Journal of molecular graphics* **1996**, *14*, 33–38.
- [70] Brooks, B. R.; Brooks III, C. L.; Mackerell Jr, A. D.; Nilsson, L.; Petrella, R. J.; Roux, B.; Won, Y.; Archontis, G.; Bartels, C.; Boresch, S. et al. CHARMM: the biomolecular simulation program. *Journal of computational chemistry* **2009**, *30*, 1545–1614.
- [71] Yoo, J.; Aksimentiev, A. Improved parametrization of Li<sup>+</sup>, Na<sup>+</sup>, K<sup>+</sup>, and Mg<sup>2+</sup> ions for all-atom molecular dynamics simulations of nucleic acid systems. *The journal of physical chemistry letters* **2011**, *3*, 45–50.
- [72] Miyamoto, S.; Kollman, P. A. Settle: An analytical version of the SHAKE and RATTLE algorithm for rigid water models. *Journal of computational chemistry* **1992**, *13*, 952–962.
- [73] Andersen, H. C. Rattle: A “velocity” version of the shake algorithm for molecular dynamics calculations. *Journal of Computational Physics* **1983**, *52*, 24–34.
- [74] Gumbart, J.; Khalili-Araghi, F.; Sotomayor, M.; Roux, B. Constant electric field simulations of the membrane potential illustrated with simple systems. *Biochimica et Biophysica Acta (BBA)-Biomembranes* **2012**, *1818*, 294–302.
- [75] Crozier, P. S.; Henderson, D.; Rowley, R. L.; Busath, D. D. Model channel ion currents in NaCl-extended simple point charge water solution with applied-field molecular dynamics. *Biophysical journal* **2001**, *81*, 3077–3089.

## Supplementary Information: Geometrically Induced Selectivity and Unidirectional Electroosmosis in Uncharged Nanopores

Giovanni Di Muccio<sup>1</sup>, Blasco Morozzo della Rocca<sup>2</sup>, Mauro Chinappi<sup>1\*</sup>

<sup>1</sup> *Dipartimento di Ingegneria Industriale,  
Università di Roma Tor Vergata,  
Via del Politecnico 1, 00133, Rome, Italy.*

<sup>2</sup> *Dipartimento di Biologia,  
Università di Roma Tor Vergata,  
Via della Ricerca Scientifica 1, 00133, Rome, Italy.*

(Dated: November 30, 2021)

### Contents:

Supplementary Note S1: Induced Debye layer capacitance for the cavity-nanopore.	p. S-2
Supplementary Note S2: Comments on the PNP-NS model	p. S-6
Supplementary Figure S1: Induced charge model and equivalent capacitance.	p. S-4
Supplementary Figure S2: Electroosmotic velocity profile and Flow rate.	p. S-7
Supplementary Figure S3: Role of prefactor on EOF and charge estimations.	p. S-8
Supplementary Figure S4: Solid and dipolar fluid models.	p. S-9
Supplementary Figure S5: Phase diagram for model dipolar fluid.	p. S-10
Supplementary Figure S6: Dielectric constant for model dipolar fluid.	p. S-11
Supplementary Figure S7: Viscosity of the model dipolar fluid in the liquid state.	p. S-12
Supplementary Figure S8: Wettability of solid-state membrane by model dipolar fluid.	p. S-13
Supplementary Figure S9: Ion diffusion coefficients and mobility for the model solution.	p. S-14
Supplementary Figure S10: Ionic currents for model system and symmetric electrolyte.	p. S-15
Supplementary Figure S11: Electric potential and Field lines for different cavity sizes	p. S-16
Supplementary Figure S12: EOF predictions for a silicon nitride nanopore.	p. S-17
Supplementary Figure S13: Net charge distribution and ionic currents for CsgG.	p. S-18
Supplementary Figure S14: WT vs Neutral Model of CsgG nanopore.	p. S-19
Supplementary Figure S15: Comparison of Induced Charge and Intrinsic Selectivity of CsgG nanopore.	p. S-20
Additional References:	p. S-21

---

\* mauro.chinappi@uniroma2.it

**SUPPLEMENTARY NOTE S1: INDUCED DEBYE LAYER CAPACITANCE**

Here we provide details on the derivation of the expression of the equivalent capacitance  $C_s$  between the lateral cavity and the pore lumen, Eq. (2) of the manuscript. We first derive the capacitance of a planar wall separating two reservoirs containing an electrolyte solution, then we extend the discussion for a cylinder and, finally, we calculate the equivalent capacitance for the cavity-nanopore system.

**Planar membrane.** The capacitance of a planar membrane case is a classical problem, see, e.g. Lauger et al. [S1], here revised for reader convenience. Let us consider the system represented in Supplementary Fig. 1a composed of an infinite neutral solid membrane of relative permittivity  $\varepsilon_S$  and thickness  $h$ , separating two reservoirs of a perfectly symmetric 1:1 electrolyte solution with relative permittivity  $\varepsilon_L$  and bulk concentration  $c_0$ . A voltage  $\Delta V$  is applied between the two reservoirs. Without loss of generality, we assumed that left side (G) is grounded. The membrane is parallel to the  $Oxy$  plane, and  $z = 0$  ( $z = -h$ ) corresponds to the interface between the right (left) reservoir and the solid membrane. The problem is hence one dimensional and all the variables depend only on the  $z$  coordinate. For small surface potential  $\zeta_w \ll k_B T/e$ , the variation of the electric potential  $\phi(z)$  into the electrolyte solution (A and G domains) is ruled by the Debye-Huckel approximation of the Poisson-Boltzmann equation [S2]

$$\frac{d^2\phi}{dz^2} = \frac{1}{\lambda_D^2} \phi, \quad (\text{electrolyte solution G}), \quad (\text{S1})$$

$$\frac{d^2\phi}{dz^2} = \frac{1}{\lambda_D^2} (\phi - \Delta V), \quad (\text{electrolyte solution A}), \quad (\text{S2})$$

where

$$\lambda_D = \sqrt{\frac{\varepsilon_0 \varepsilon_L k_B T}{2(\nu e)^2 c_0}}$$

is the Debye length,  $\varepsilon_0$  the vacuum electrical permittivity,  $\nu$  the valence of the ions (1 in our case),  $e$  the elementary charge,  $k_B$  the Boltzmann constant and  $T$  the temperature. Inside the membrane, instead, the Poisson equation reduces to

$$\frac{d^2\phi}{dz^2} = 0, \quad (\text{membrane S}). \quad (\text{S3})$$

Equations (S1)-(S3) are solved with the following boundary conditions,

$$\phi(z) = 0 \quad \text{for} \quad z \rightarrow \infty, \quad (\text{S4})$$

$$\phi(z) = \Delta V \quad \text{for} \quad z \rightarrow -\infty, \quad (\text{S5})$$

$$\varepsilon_S \frac{d\phi_S}{dz} \Big|_{z=0} = \varepsilon_L \frac{d\phi_G}{dz} \Big|_{z=0}, \quad (\text{S6})$$

$$\varepsilon_S \frac{d\phi_S}{dz} \Big|_{z=-h} = \varepsilon_L \frac{d\phi_A}{dz} \Big|_{z=-h}, \quad (\text{S7})$$

where (S6) and (S7) impose the continuity of the normal component of the electrical displacement vector  $\mathbf{D} = \varepsilon_0 \varepsilon_{L/S} \mathbf{E}$  at the interfaces between the domains G and S, Eq. (S6), and A and S, Eq. (S7), respectively. The solution of the system (S1)-(S3) with the boundary conditions (S4)-(S7) is composed of two exponential branches in the liquid reservoirs and a linear branch in the solid membrane. In particular, we get the following solution

$$\phi(z) = \zeta_w \exp\left[-\frac{z}{\lambda_D}\right], \quad \text{for } z \geq 0 \quad (\text{electrolyte solution G}), \quad (\text{S8})$$

$$\phi(z) = \Delta V - \zeta_w \exp\left[\frac{(z+h)}{\lambda_D}\right], \quad \text{for } z \leq -h \quad (\text{electrolyte solution A}), \quad (\text{S9})$$

$$\phi(z) = \zeta_w - \left(\frac{\Delta V - 2\zeta_w}{h}\right) z, \quad \text{for } -h < z < 0 \quad (\text{membrane S}). \quad (\text{S10})$$

where

$$\zeta_w = \left(\frac{\varepsilon_S}{\varepsilon_L}\right) \left(\frac{\lambda_D}{h}\right) \left(\frac{\Delta V}{1 + \frac{2\lambda_D}{h} \frac{\varepsilon_S}{\varepsilon_L}}\right) \quad (\text{S11})$$

is the magnitude of the difference between the bulk potential and the surface potential. In essence,  $\zeta_w$  is the magnitude of the induced surface potential.

From now on, since the system is symmetric with respect to the membrane (e.g. the two electrolyte solutions in the reservoirs G and A are identical), we will focus only on the ground reservoir G. Once  $\phi(z)$  is known, the charge density in the liquid,  $\rho_{el}(z)$ , is obtained as

$$\rho_{el}(z) = -\frac{\varepsilon_0 \varepsilon_L \zeta_w}{\lambda_D^2} \exp\left[-\frac{z}{\lambda_D}\right], \quad \text{for } z \geq 0, \quad (\text{S12})$$

where, again, we are using the Debye-Hückel approximation. The region in the electrolyte solution domain where the charge accumulates under the action of the applied voltage  $\Delta V$  is known as induced Debye layer (IDL, colored area in Supplementary Fig. S1 and manuscript Fig. 1c). Integrating Eq. (S12) in the liquid reservoir, the total charge  $q$  for unit of surface in the IDL is

$$q_{pla} = \int_0^\infty \rho_{el}(z) dz = -\frac{\varepsilon_0 \varepsilon_L \zeta_w}{\lambda_D} = -\left(\frac{\varepsilon_0 \varepsilon_S}{h}\right) \left(\frac{\Delta V}{1 + \frac{2\lambda_D}{h} \frac{\varepsilon_S}{\varepsilon_L}}\right). \quad (\text{S13})$$

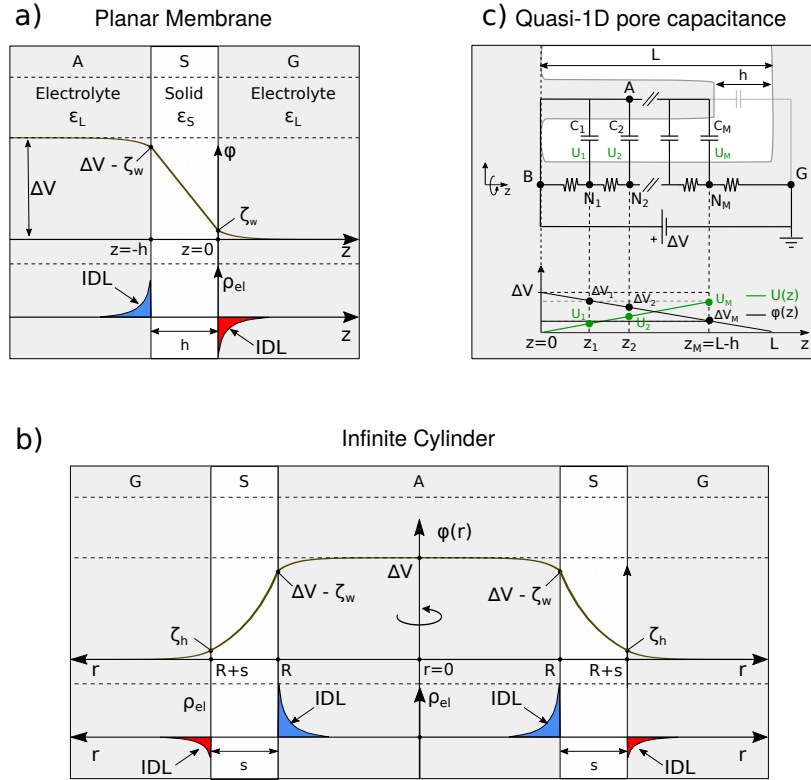
so that the capacitance per unit area of the membrane is

$$C_{pla} = \left|\frac{q_{pla}}{\Delta V}\right| = \frac{\varepsilon_0 \varepsilon_S}{h} \left(1 + \frac{2\lambda_D}{h} \frac{\varepsilon_S}{\varepsilon_L}\right)^{-1}. \quad (\text{S14})$$

For  $\lambda_D \ll h$ , Eq. (S14) reduces to the formula for the geometric capacitance per unit area of a planar capacitor of height  $h$ ,

$$C_{pla} = \frac{\varepsilon_0 \varepsilon_S}{h}. \quad (\text{S15})$$

This is not surprising, indeed, for  $\lambda_D \ll h$ , the charge in the Debye layer accumulates in a very thin region close to the liquid-solid interface and  $\zeta_w \ll \Delta V$ , see Eq. (S11). In our system,  $\lambda_D$  and  $h$  are



**Supplementary Figure S1. Induced charge model and equivalent cavity-nanopore capacitance.** **a-b)** Sketches of the electrical potential  $\phi$  and net charge distributions  $\rho_{el}$  induced by a voltage drop  $\Delta V$  across **a)** a planar membrane and **b)** an infinite cylinder, separating two electrolyte solutions (A and G). The continuity of the electrical displacement field at the solid-liquid interfaces drives the formation of Induced Debye Layer (IDL) of opposite charge, resulting in a capacitance. **c)** Circuit model employed for calculating the equivalent capacitance  $C_s$  between the pore lumen and the lateral cavity. The lower panel report the electric potential  $\phi(z)$  (black line) that linearly decreases from  $\Delta V$  (point B,  $z = 0$ ) to 0 (point G,  $z = L$ ) and the potential difference  $U(z)$  (green line) between the lateral cavity and the pore lumen that linearly increases from 0 (point B,  $z = 0$ ) to  $\Delta V(L - h)/L$  (node  $N_m$ ,  $z = L - h$ ).

comparable, nevertheless, considering a 1M water solution  $\varepsilon_L = 78$  of a 1:1 electrolyte at  $T = 300$  K, ( $\lambda_D = 0.304$  nm) and a  $h = 1$  nm thick membrane with  $\varepsilon_S = 1$ , the second factor of Eq. (S14) is  $\simeq 0.99$ . So, again, Eq. (S15) is a very good approximation for the capacitance per unit surface.

As a final comment, we note that, for an applied voltage  $\Delta V = 1$  V, Eq. (S11) predicts a value  $\zeta_w \approx 3.4$  mV that is lower than the thermal voltage  $k_B T/e = 25$  mV, implying that the Debye-Hückel approximation is valid even for relatively large voltages (compared to those often employed in nanopore experiments).

**Infinite cylinder.** Applying a similar approach, we derived an analogous result for a cylindrical electrolytic capacitance. Let us consider an infinite insulating cylindrical membrane of inner radius  $R$  and outer radius  $R + s$  separating two electrolyte solutions (A and G), see Supplementary Fig. 1b. Outer domain is grounded (G) while the potential on the cylinder axis is  $\Delta V$ . As in the planar case, in principle it is possible to solve

the Debye-Hückel approximation of the Poisson-Boltzmann equation in the two domains A and G and the Poisson equation in the membrane domain S, Supplementary Fig. 1b. However, for  $\lambda_D \ll R$  and  $\lambda_D \ll h$ , the IDL is thin compared to the cylindrical membrane size. So the capacitance for unit of length of the system can be approximated to

$$C_{cyl} = \frac{2\pi\epsilon_0\epsilon_S}{\ln\left(1 + \frac{s}{R}\right)}, \quad (\text{S16})$$

that, similarly to the planar case, is the geometrical capacitance for unit of length for a cylindrical capacitor with dielectric constant  $\epsilon_S$ , inner radius  $R$  and outer radius  $R + s$ .

**Equivalent cavity-nanopore cylindrical capacitance.** For the estimation of the capacitance between the nanopore lumen and the cavity surrounding the entrance, we developed the quasi-1D model sketched in Supplementary Fig. S1c. The white domain in Supplementary Fig. S1c corresponds to half-section of the solid membrane separating the two electrolyte reservoirs. The nanopore connects the two reservoirs and its axis lies on the  $z$  axis of the coordinate system. In our circuit model, the branch BG corresponds to the pore lumen and the point A to the lateral cavity. The point G is connected to the ground and a potential  $\Delta V$  is applied at the point B (left pore entrance,  $z = 0$ ). We assume that the potential inside the lateral cavity is uniform and equal to  $\Delta V$ , i.e., equal to the potential at the left pore entrance. Instead, the potential  $\phi(z)$  along the nanopore linearly decays from  $\Delta V$  to zero, when moving from left entrance ( $z = 0$ ) to right entrance ( $z = L$ )

$$\phi(z) = \Delta V \left(1 - \frac{z}{L}\right). \quad (\text{S17})$$

The difference in the potential between the pore lumen and the cavity (point A) leads to an accumulation of charges inside the pore lumen that can be estimated as follows. Let us divide the branch BG into  $M$  segments so that  $M - 1$  intermediate nodes  $N_k$  exist, each one at potential  $V_k = \phi(z_k)$ , with  $z_k = k\Delta z$  and  $\Delta z = (L - h)/M$ , with  $L$  the pore length and  $h$  the membrane thickness in the cavity, see Supplementary Fig. S1c. For each node  $N_k$ , we assume a cylindrical capacitor  $C_k$  of length  $\Delta z$ , subjected to a potential difference  $U_k = \Delta V - V_k$ . The charge  $q_N$  is then the sum of the charges accumulated in each  $C_k$  capacity,

$$q_N = \sum_{k=1}^M C_{cyl} U_k \Delta z, \quad (\text{S18})$$

with  $C_{cyl} = C_k/\Delta z$  the cylindrical capacitance per unit length.

In the limit  $M \rightarrow \infty$ , we have  $z_k \rightarrow z$ ,  $U_k = U(z)$  and the summation becomes the integral

$$q_N = \int_0^{L-h} C_{cyl}(z) U(z) dz. \quad (\text{S19})$$

In general  $C_{cyl}(z)$  depends on the radius of the pore, see Eq. (S16), and hence, for a generic axial-symmetric pore shape, it is a function of  $z$ . However, in our case the pore is cylindrical so  $C_{cyl}$  is constant along the pore and Eq. (S19) can be analytically worked out as

$$q_N = C_{cyl} \int_0^{L-h} dz U(z) = \frac{1}{2} \frac{(L-h)^2}{L} C_{cyl} \Delta V \quad (\text{S20})$$

that, using Eq. (S16), reduces to

$$q_N = \frac{\pi\epsilon_0\epsilon_S}{L} \frac{(L-h)^2}{\ln\left(1 + \frac{s}{R}\right)} \Delta V, \quad (\text{S21})$$

and consequently the equivalent capacitance is

$$C_s = \frac{\pi\epsilon_0\epsilon_S}{L} \frac{(L-h)^2}{\ln\left(1 + \frac{s}{R}\right)}. \quad (\text{S22})$$

In the Eq. (2) of the manuscript we added a prefactor  $(L - 4\lambda_D)/L$  to take into account the effect of pore entrances. Indeed, as shown in Fig. 1e of the manuscript, the deformation of the charge distribution at the pore entrance extends for around  $2\lambda_D$  inside the pore. Since in our systems, for 2M ion concentration  $\lambda_D \simeq 2 \text{ \AA}$ , for long pores (e.g. the  $L = 30 \text{ \AA}$  pore discussed in Fig. 1) this additional factor corresponds to a correction of  $\simeq 25\%$  on pore lumen charge  $q_N$  and electroosmotic flow rate  $Q_w$ .

**SUPPLEMENTARY NOTE S2: COMMENTS ON THE PNP-NS MODEL**

To achieve practical analytical solutions such as Eq. (4) and Eq. (8), we needed to introduce several hypotheses in the electrohydrodynamical model. Here, for clarity, we revise the overall continuum theoretical framework on which our work is based. This framework is quite standard, we report here the main concepts, focusing on some hypotheses we find important to discuss, referring the interested readers to other sources such as [S2, S3].

As a first step, we present the continuum model. In electrohydrodynamics of electrolyte solutions, continuum models are derived by the momentum, mass, energy and species balance equations plus the Poisson equation for electrostatics. We indicate as  $c_\alpha$  the ion concentration, with  $\alpha \in [1, N_s]$  where  $N_s$  is the number of ion species. The first hypothesis we introduce is the dilution, *i.e.*, we assume that the concentration of ions is so low that the properties of the solutions (*e.g.* viscosity  $\eta$ , relative permittivity  $\varepsilon_L$ , density  $\rho$ ) are not affected by  $c_\alpha$ . Moreover, we assume that the solution is incompressible, hence the pressure  $p$  does not affect  $\rho$ . Then, we also assume that the variation of temperature  $T$ , due for instance to viscous dissipation or to heat flux at system boundaries, is so small that it doesn't affect the solution properties ( $\rho$ ,  $\eta$ ,  $\varepsilon_L$ , etc etc). This last hypothesis allows to decouple the energy equation from the others, *i.e.*, mass, species and momentum balance can be solved without considering the temperature distribution. Dilution has two other relevant implications: i) the terminal velocity of a single ion of the solution due to an electric field  $\mathbf{E}$  is strictly proportional to the electric field with the proportionality constant not affected by ion concentration  $c_\alpha$ . ii) the diffusion contribution to the particle flux can be modelled using Fick's law with diffusion coefficient  $D$  not depending on  $c_\alpha$ . (These two claims are linked by fluctuation-dissipation relation). If we use, as is common for simple fluids, the Newtonian model for viscous stresses, the final set of equation reads

$$\frac{\partial c_\alpha}{\partial t} + \mathbf{u} \cdot \nabla c_\alpha = D \nabla^2 c_\alpha + c_\alpha \mu \nabla^2 \phi \quad (\text{S23})$$

$$\frac{\partial \mathbf{u}}{\partial t} + \mathbf{u} \cdot \nabla \mathbf{u} = \frac{1}{\rho} (\eta \nabla^2 \mathbf{u} - \nabla p - \rho_e \nabla \phi) , \quad (\text{S24})$$

$$\nabla \cdot \mathbf{u} = 0 , \quad (\text{S25})$$

$$\nabla^2 \phi = -\frac{\rho_e}{\varepsilon_L} , \quad (\text{S26})$$

where  $\mathbf{u}$  and  $\phi$  are the fluid velocity and electrostatic potential and  $\rho_e$  electric charge density which can be written as a function of the ionic species concentration  $c_\alpha$  by

$$\rho_e = \sum_{\alpha=1}^{N_s} c_\alpha \nu_\alpha e , \quad (\text{S27})$$

where  $\nu_\alpha e$  is the charge of species  $\alpha$ , expressed in terms of the elementary charge  $e$ , so, *e.g.*  $\nu_\alpha = +1$  for  $K^+$  and  $\nu_\alpha = -1$  for  $Cl^-$ . At sufficiently small scales, typical of nanopores, the Reynolds number is small and it is safe to neglect nonlinear and time dependent terms, *i.e.*, the left-hand side of Eq. (S24), leading to the Stokes equation. For generic geometries, the system (S23)-(S26) needs to be solved numerically. However, a specific solution exists in the Debye-Hückel approximation for the cylindrical pores whose surface is at a wall potential  $\zeta_w$  under the action of an external electrical field parallel to the pore axis. This solution can be expressed in terms of Bessel functions [S3, S4], but, for  $\lambda_D \ll R$ , in essence the velocity profile is quite similar to a plug flow whose magnitude in the center of the channel is given by the Helmholtz-Smoluchowski electroosmotic velocity (see also Eq. (5) of the manuscript)

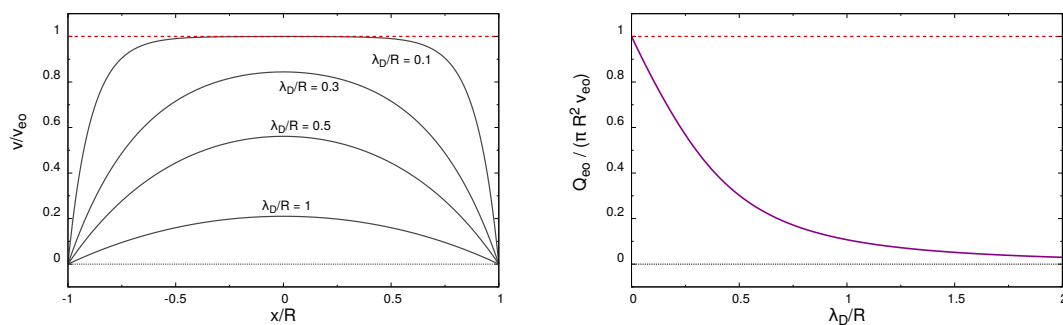
$$|v_{eo}| = \frac{\varepsilon_0 \varepsilon_L \zeta_w}{\eta} \frac{\Delta V}{L} , \quad (\text{S28})$$

while the charge profile is zero everywhere, except for a thin region close to the wall. As  $\lambda_D/R$  decreases, the charge accumulated in the channel converges to the product of pore surface  $2\pi RL$  times the surface charge of a planar Debye layer  $\varepsilon_0 \varepsilon_L \zeta_w / \lambda_D$ .

Hence, in the derivation of our model we have two different sets of hypotheses. On the one hand, since we rely on PNP-NS model, we implicitly assume all the above cited hypotheses (continuum, dilution,

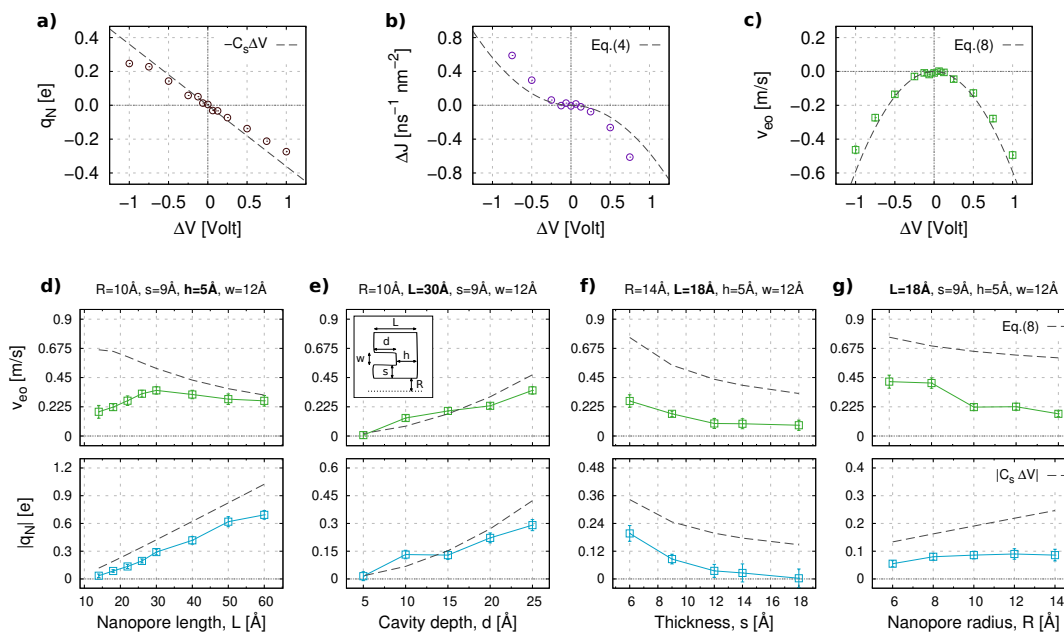
incompressibility). Although the reliability of these assumption at the nanoscale is *a priori* questionable, several studies reported an unexpected capability of PNP-NS model to quantitatively capture the current through nanopores. For instance, in Bonome et al. [S5], an analytical electroosmotic model based on ideal EOF in a cylindrical channel was shown to be able to capture the order of magnitude of EOF measured from MD simulation in an  $\alpha$ HL nanopore. Other remarkable examples of successful application of continuum models to nanopores are the recent study by Willems et al [S6] where the EOF through a large biological pore is calculated using a PNP-NS model and the work by Wilson et al. [S7] where a steric exclusion model based on Ohm law allowed to calculate current blockades for proteins confined into a solid-state nanopore, biological channels and blockade currents produced by DNA homopolymers in MspA, showing impressive agreement with all-atoms MD data. In both these works, a crucial ingredient to improve the quantitative matches of the continuum model with experiments or all-atoms MD was the additional calibration of the transport coefficient (*e.g.* dependence of ion mobility on the distance from the wall and on the ion concentration). However, the qualitative trends are expected to be well captured also without these more detailed models, see, *e.g.* Supporting Information of Willems et al [S6].

The second class of hypotheses, instead, enters after PNP-NS and concerns the above mentioned limit for  $\lambda_D \ll R$ . As shown in Fig. S2, these hypotheses tend to overestimate both the EOF and the charge accumulated in the nanopore.

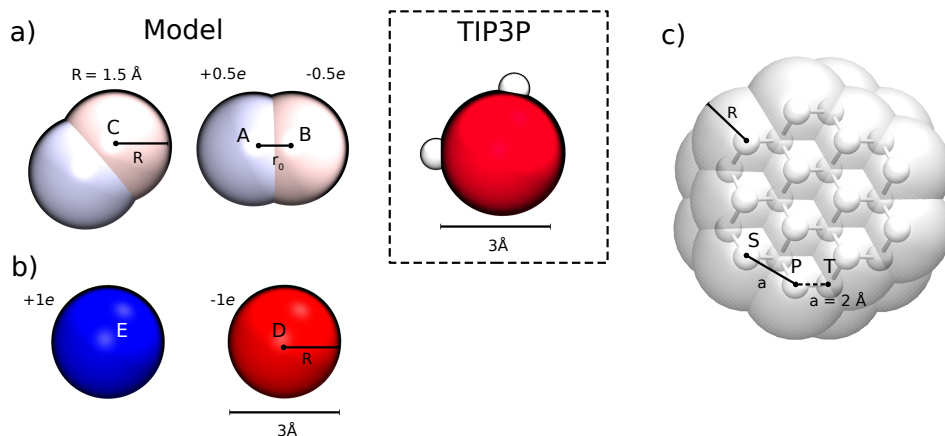


**Supplementary Figure S2. Electroosmotic velocity profile and Flow rate.** a) Electroosmotic velocity profile as a function of radial coordinate  $r$  for different values of  $\lambda_D/R$ . The curves refer to the classical analytical solution in a cylindrical pore of radius  $R$  with constant  $\zeta_w$ -potential at the wall and external electric field applied parallel to the pore axis. More specifically,  $v = v_{eo} [1 - I_0(r/\lambda_D)/I_0(R/\lambda_D)]$  where  $I_0$  is the modified Bessel function of order 0 [S3] and  $v_{eo}$  is the Helmholtz-Smoluchowski electroosmotic velocity [S3]. It is evident that for  $\lambda_D/R \rightarrow 0$ , the profile tends to a plug flow of velocity  $v_{eo}$ . b) Flow rate through a cylindrical pore as a function of  $\lambda_D/R$ , obtained integrating the velocity profiles  $v(r)$  on the pore section. In the limit  $\lambda_D/R \rightarrow 0$ , mass flow rate coincides with the plug flow  $Q_{eo} = \pi R^2 v_{eo}$ , Eq. (5) of the manuscript.

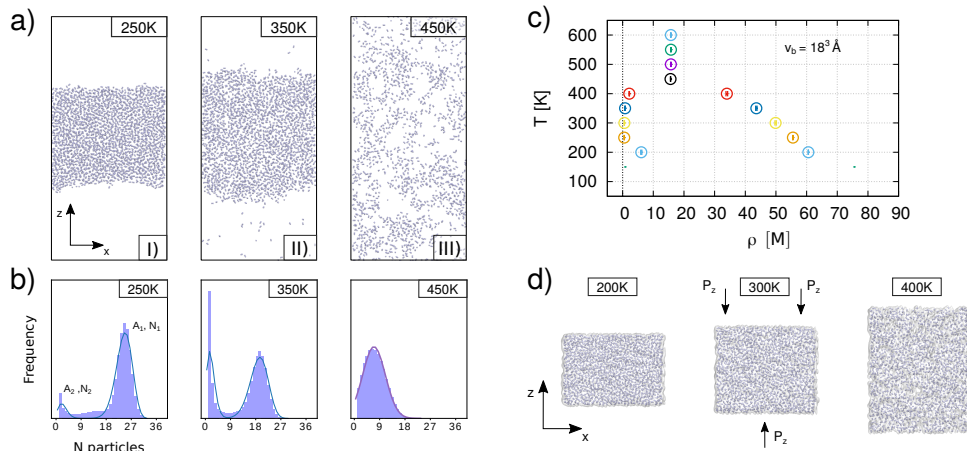
The above cited literature strongly suggested that our model would be able to describe the qualitative trends or to capture the order of magnitude of the selectivity and EOF. The fact that we also get a nice qualitative agreement with simulation data was not *a priori* expected. One possibility is that some fortuitous compensation happens. For instance, various overestimations of the EOF due to the assumption that  $\lambda_D \ll R$  may be compensated by the prefactor  $(L - 4\lambda_D)/L$  introduced to take into account the effect of pore entrances (see Supplementary Note S1). Nevertheless, also without the pore entrance prefactor, our model provides predictions that are quite close to the simulation data (the maximum difference is a factor 3 and occurs for very short pores where entrance effects are more relevant) see Supplementary Fig. S3, where the same MD data of Fig. 3 of the manuscript are reported together with model prediction without pore entrance prefactor.



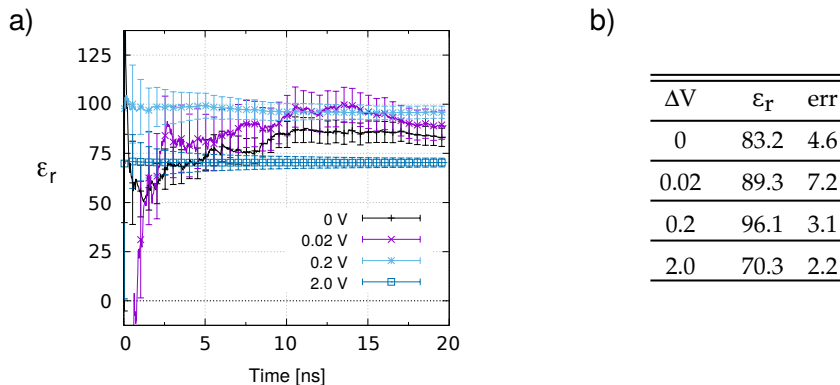
**Supplementary Figure S3. Role of prefactor on EOF and charge estimations.** The MD data reported are the same as in Fig. 3 of the manuscript while the lines refer to the theoretical prediction obtained without the prefactor  $(L - 4\lambda_D)/L$  introduced to consider the effect of pore entrance. In all cases, the model is able to capture the order of magnitude of EOF. The maximum difference is of about a factor 3 and occurs for short pores (see *e.g.* panels **f**) and **g**),  $L = 18 \text{ \AA}$  and panel **a**) for  $L < 25 \text{ \AA}$ .



**Supplementary Figure S4. Solid and dipolar fluid models.** **a)** Diatomic particle forming our dipolar model fluid (the solvent). Each molecule is composed of two atoms covalently bound via a harmonic potential with spring constant  $k_b = 450 \text{ kcal}/(\text{mol } \text{\AA}^2)$  and equilibrium bond length  $r_0 = 1 \text{ \AA}$ . The two atoms carry opposite charges  $q^+ = 0.5e$  and  $q^- = -0.5e$ , giving an overall neutral molecule with a dipole intensity  $|p| = 0.05 e \cdot \text{nm}$ . The mass of each atom is  $m = 10 \text{ Da}$ . Non-bonded interactions, e.g. between atom A and atom C, are modelled using a standard Coulomb potential for the electrostatics forces and a Lennard-Jones (LJ) potential with parameters  $\epsilon_{LL} = 0.1 \text{ kcal/mol}$ ,  $\sigma_{LL} = 2.68 \text{ \AA}$ . On the right, a TIP3P water is drawn to scale. **b)** Ions are formed by atoms with charge  $q^\pm = \pm 1e$  and mass  $m_I = 40 \text{ Da}$ . Non bonded interactions are again modelled as electrostatic plus LJ potentials. The LJ parameters for the ion-solvent interaction are the same as for solvent-solvent, while for ion-ion interaction we used but  $\sigma_I = 3.125 \text{ \AA}$ . The slightly larger value  $\sigma_I$  compared to the solvent-solvent  $\sigma_{LL}$  was used to avoid the aggregation of ions. The resulting electrolyte solution corresponds to a fully dissociated binary symmetric salt in a symmetric liquid. **c)** Solid crystal forming the membrane. Top view of the hexagonal closest packed solid lattice, only two atomic layers are shown. Atoms are uncharged, with mass  $m_S = 10 \text{ Da}$  and equilibrium distance of  $a = 2 \text{ \AA}$ . To keep the material solid, atoms are harmonically bonded to three nearest neighbors belonging to the upper and lower planes (see e.g. atoms P and T) for a total of six bonds for each atom, with equilibrium distance  $r_{0,s} = a$ , and spring constant  $k_b = 450 \text{ kcal}/(\text{mol } \text{\AA}^2)$ . LJ model is used for non-bonded interactions with  $\sigma_{SS} = a$  and  $\epsilon_{SS} = 1 \text{ kcal/mol}$ . In nanopore simulations the atoms are also constrained by a harmonic spring of  $k_c = 100 \text{ kcal}/(\text{mol } \text{\AA}^2)$ . LJ parameters for solid-liquid interaction are  $\epsilon_{SL} = 0.8\epsilon_{LL}$  and  $\sigma_{SL} = \sigma$ . The value of  $\epsilon_{SL}$  can be modified to control the wettability, see Supplementary Fig. 8. Images are made using VMD [S8].



**Supplementary Figure S5. Phase diagram for model dipolar fluid.** NVT simulations of 20 000 dipolar molecules in a triperiodic box ( $L_x = L_y = 90 \text{ \AA}$ ,  $L_z = 270 \text{ \AA}$ ) were run at different temperatures  $T$ . A preliminary 200 ps pre-heating at 2500 K is followed by a 500 ps cooling to the final  $T$ . The pre-equilibration stage is used to bring the system away from local energy minima induced by the initial artificial arrangement of the molecules. Langevin thermostat with damping coefficient  $0.05 \text{ ps}^{-1}$  is used in all the runs. The equilibrated system is then sampled for 4 ns, saving the coordinates every 20 ps. **a)** Snapshots of the system at three representative  $T$ . **b)** Density distribution computed by dividing the simulation cell in cubic blocks of volume  $v_b = 18^3 \text{ \AA}^3$  and counting the molecules in each block at every sampled frame. Solid lines refer to a bimodal Poisson fit (for bimodal distributions) or to Gaussian fit (for unimodal distribution). **c)** Density-temperature state diagram. For each temperature, circles correspond to the peaks of the fitted distribution with error bars being the corresponding fit errors. Unimodal distributions are found for  $T > 400 \text{ K}$  indicating that the critical temperature  $T_c$  is between  $400 < T_c < 450 \text{ K}$ . Number density is reported in mol/L, for  $T = 250 \text{ K}$  we get  $\rho \simeq 55.5 \text{ mol/L}$ , a value very similar to water number density. **d)** Final frame of 12 ns NPT runs ( $P = 1 \text{ bar}$ ) at different temperatures, showing that our fluid is in a liquid state in the interval  $200 \leq T \leq 400 \text{ K}$ . Panels **a** and **d** were made using VMD [S8]. Statistical analyses of density distributions were done using Python modules Scipy [S9] and Matplotlib [S10].



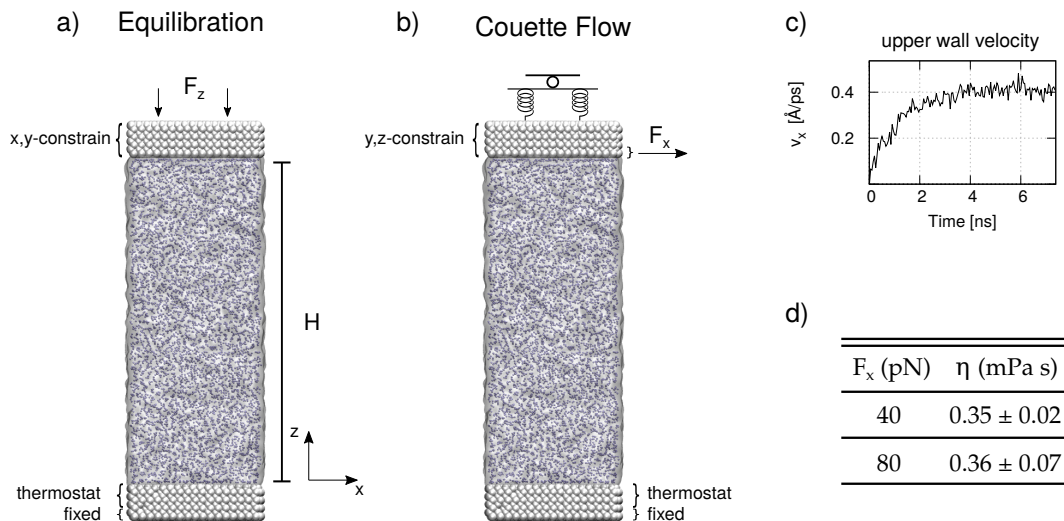
**Supplementary Figure S6. Dielectric constant for model dipolar fluid.** a) The plot represents the MD relative permittivity estimation, using two different methods, as a function of the sampling time, for four different applied voltages  $\Delta V$ . The simulation set-up is a rectangular box of size  $L_x = L_y = 80 \text{ \AA}$ ,  $L_z = 140 \text{ \AA}$ . After an NPT equilibration ( $T = 250 \text{ K}$ ,  $P = 1 \text{ atm}$ ), a 25 ns NVT production run is started and frames are sampled every 20 ps. The first 5 ns were discarded. The first permittivity estimation method is a non-equilibrium approach where a constant electric field  $\mathbf{E} = (0, 0, E_z)$ , corresponding to a potential  $\Delta V = -L_z E_z$  is applied to the system. Following [S11, S12], the relative permittivity  $\epsilon_r$  is computed as

$$\epsilon_r = 1 + \frac{\langle M_z \rangle}{\epsilon_0 E_z \Gamma},$$

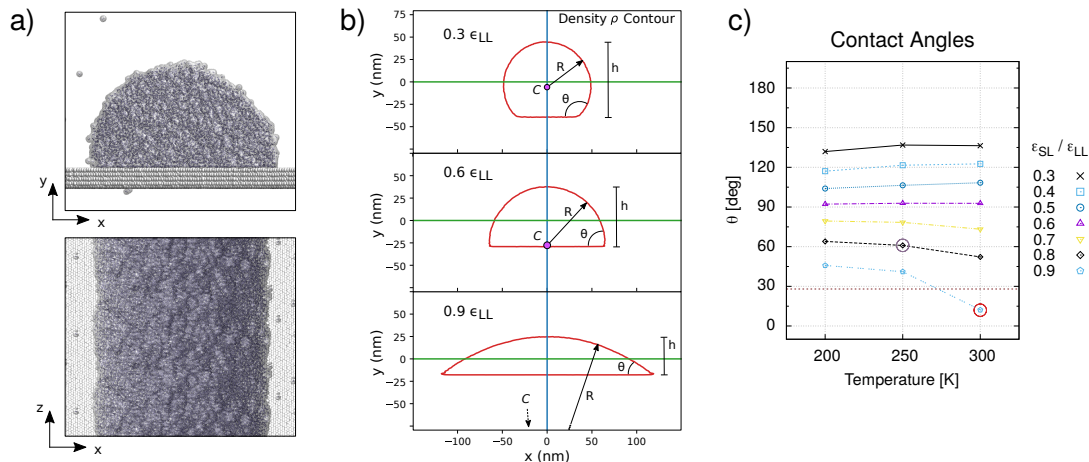
with  $\epsilon_0$  the vacuum permittivity, with  $M_z$  total dipole moment in the  $z$ -direction and  $\Gamma = L_x L_y L_z$  the volume of the system. In the second method (black points) no electrical field is applied to the system, and we computed the dielectric constant as [S12]

$$\epsilon_r = 1 + \frac{\langle M_z^2 \rangle}{\epsilon_0 k_B T \Gamma},$$

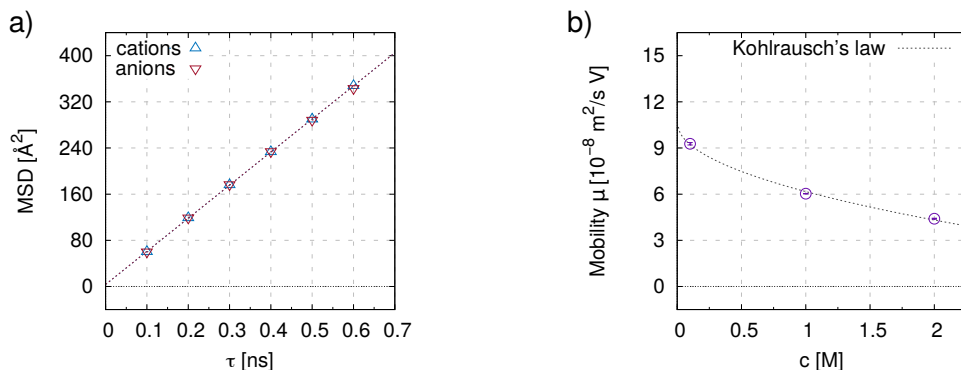
with  $k_B$  the Boltzmann constant and  $T$  the temperature. It is apparent from the figure that the estimation of  $\epsilon_r$  reached a plateau for all the simulated systems. Each data point is calculated as the average over the previous frames. The error bars represent the standard errors of the respective estimator, computed over the previous frames. The final estimated values, after 20 ns, are reported in panel b). VMD [S8] is used to calculate  $M_z$  and  $M_z^2$  at each frame.



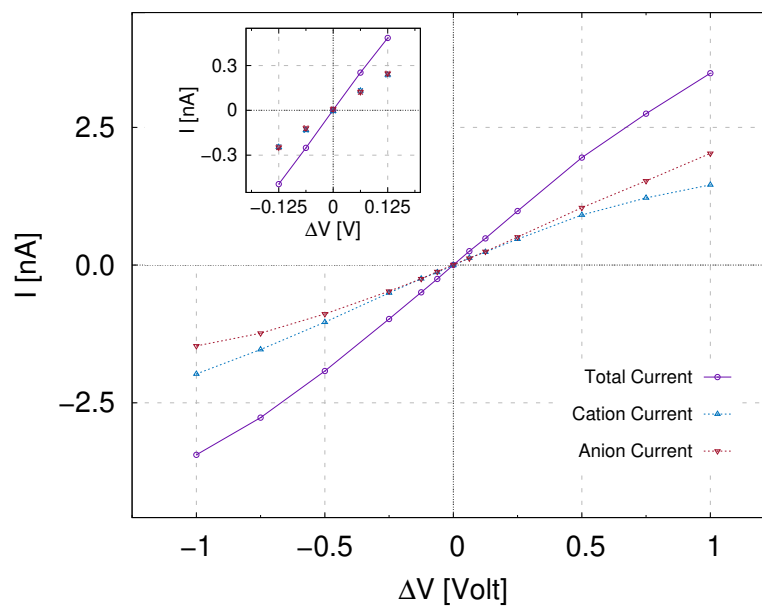
**Supplementary Figure S7. Viscosity of the model dipolar fluid in the liquid state.** The system is composed by 11 269 liquid molecules, confined between two flat solid slabs, each one composed of 6 936 atoms. The bottom layer of the lower wall is fixed, while atoms from the other layers are thermostated at  $T = 250$  K (Langevin, damping  $5 \text{ ps}^{-1}$ ). During the equilibration, panel **a**), the atoms of the top layers are constrained on the  $x$ - $y$  plane, while a force  $F_z$ , corresponding to a pressure of 1 atm, is applied along the  $z$ -axis to the topmost layer, until the liquid reaches a stable height  $H = 134.69 \pm 0.02 \text{ \AA}$  (density  $\rho = 55.5 \text{ mol/L}$ ). The production run is performed by applying a constant force  $F_x$  to the top solid layer in contact with the liquid, panel **b**). During the production run, the atoms of the top layers are harmonically constrained on their  $y - z$  positions, letting them free to move along the  $x$  direction. The top solid slab reaches a steady state velocity  $v_x$  after about 6 ns, panel **c**). After, a 2 ns sampling is performed to compute the velocity profile  $v_x(z)$  of the liquid, saving the coordinates every 50 ps. For each frame, the velocity profile  $v_x(z)$  is computed by dividing the volume height  $H$  into slabs of thickness  $\Delta z = 1 \text{ \AA}$ , using the following procedure: i) the atoms inside the slab at the frame  $f$  are selected; ii) the  $x$ -velocity of each atom  $k$  is computed as  $v_k = (x_k(f+1) - x_k(f-1))/(2\Delta t)$ , with  $x_k(f \pm 1)$   $x$ -position of the atom  $k$  at the frame  $f \pm 1$ , and  $\Delta t$  sampling interval; iii) the average velocity in the slab is computed as the average of the velocity of the atoms in the slab. By averaging over all frames after the transient, we get a linear profile  $v_x(z)$  whose slope  $\gamma$  is related to the viscosity of the liquid  $\eta = F_x/A\gamma$ , with  $A$  surface area where the shear forcing  $F_x$  is applied. **d**) Values of viscosity  $\eta$  estimated at two different  $F_x$ .



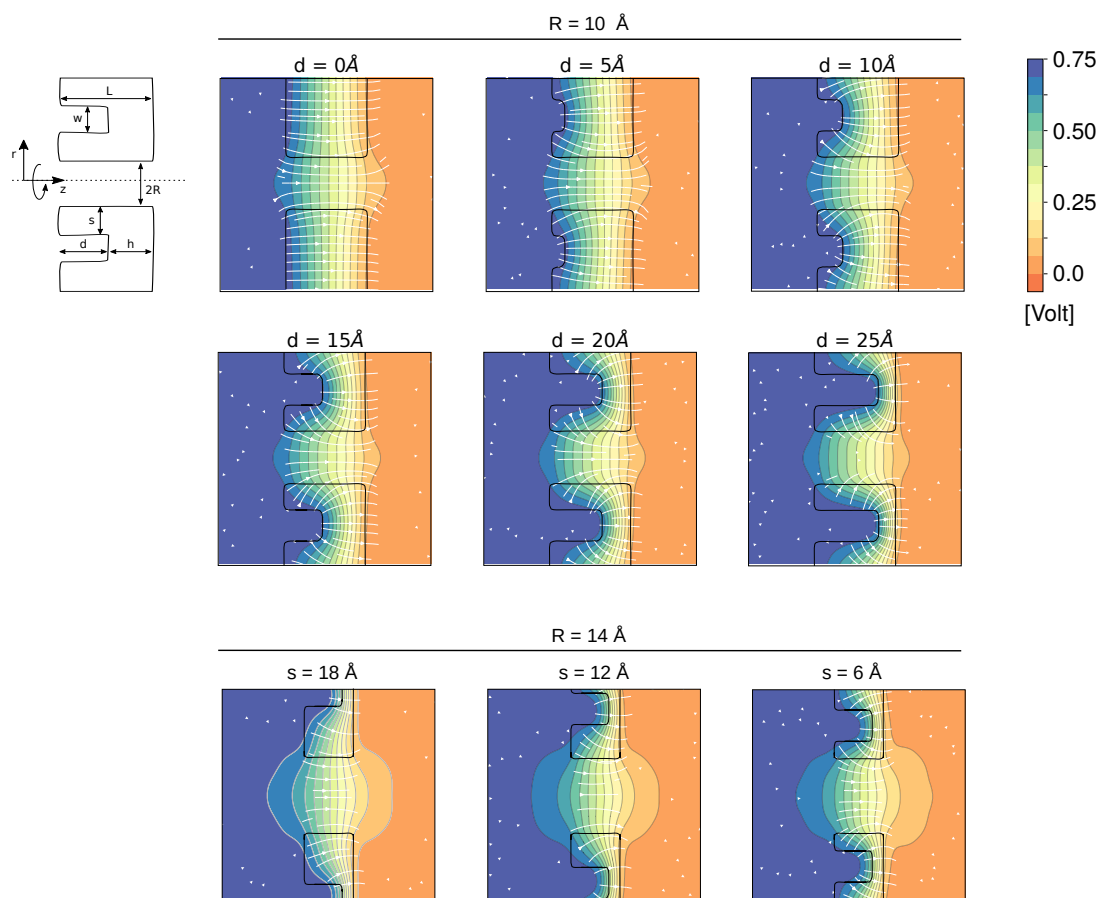
**Supplementary Figure S8. Wettability of solid-state membrane by model dipolar fluid. a)** System set-up for cylindrical droplet protocol. A liquid drop formed by 15 000 fluid molecules is in contact with a solid slab ( $L_x = 200 \text{ \AA}$ ,  $L_y = 60 \text{ \AA}$ , 48 000 uncharged atoms, only the central portion of the system, where the drop is placed, is reported). Each solid atom is weakly constrained to its lattice position (harmonic spring constant  $k_b = 100 \text{ kcal}/(\text{mol \AA}^2)$ ). Wetting can be tuned with the liquid-solid LJ parameter  $\epsilon_{SL}$ . The solid is eight atomic layers thick, so that the slab  $z$ -height is greater than the LJ cutoff radius ( $r_c = 12 \text{ \AA}$ ). Tri-periodic boundary conditions have been applied. To estimate the contact angle  $\theta$ , NVT simulations are performed (2 ns equilibration, 4 ns production). During the production runs, thermostat is applied only to the solid membrane. **b)** A procedure similar to one reported in [S13] is used to calculate  $\theta$ . In brief, we first calculated a 3D density map of the liquid, discretizing the system in cells of  $1 \times 1 \times 1 \text{ \AA}^3$  and averaging over time, at each step the droplet is centered on its center of mass to compensate any collective movements of the fluid parallel to the solid surface. After, we computed a 2D density map by averaging over the  $z$ -planes. Droplet boundary is defined as the isodensity contour lines corresponding to the half-mode of the 2D density distribution (red contour), and  $\theta$  is calculated as  $\theta = \arccos(1 - h/R)$  with  $h$  and  $R$  the nominal height and the radius of the droplet. **c)** Contact angle  $\theta$  as a function of the temperature  $T$  for different liquid-solid interaction  $\epsilon_{LS}$ . The red circled point under the dashed line indicates that the liquid uniformly wets the entire surface. For our nanopore simulations, we used a  $\epsilon_{SL} = 0.8\epsilon_{LL}$ , corresponding to an hydrophilic surface with  $\theta \simeq 60^\circ$ , conditions indicated by the grey circled point.



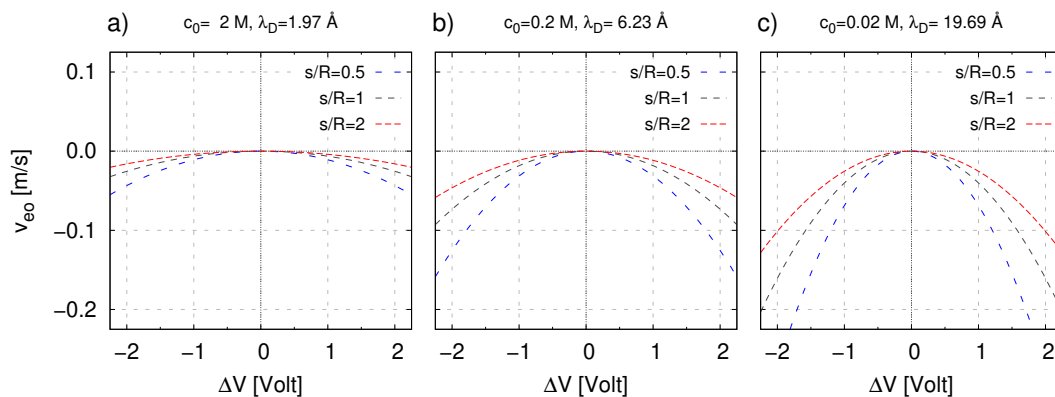
**Supplementary Figure S9. Ion diffusion coefficients and mobility for the model symmetric electrolyte solution.** **a)** Mean squared displacement (MSD) as a function of simulation time, for a 2M triperiodic system (313 292 total atoms, 11 280 ions). After an NPT equilibration ( $T = 250 \text{ K}$ ,  $P = 1 \text{ atm}$ ), a 4 ns NVT production run is performed, sampling particle positions every 100 ps. The first nanosecond is discarded and then the MSD is computed over the remaining frames by using VMD scripts [S8]. The slope of the curve is related to the diffusion coefficient  $D$  of the ion in the electrolyte solution by the relation  $\text{MSD}(\tau) = 6D\tau$  [S14], resulting in the fitted values  $D_+ = 95.6 \pm 0.21 \text{ \AA}^2/\text{ns}$  and  $D_- = 94.4 \pm 0.73 \text{ \AA}^2/\text{ns}$ . From the diffusion coefficient, the ion mobility is estimated via the Einstein relation  $\mu_{\pm} = q_{\pm}D_{\pm}/(k_B T)$ . Results at different concentrations are shown in **b)**. As predicted by Kohlrausch law [S15],  $\mu(c) = \mu_0 - K\sqrt{c}$ , the ionic mobility decreases with increasing ion concentration, with  $\mu_0$  the mobility at infinite dilution, and  $K$  an empirical constant.



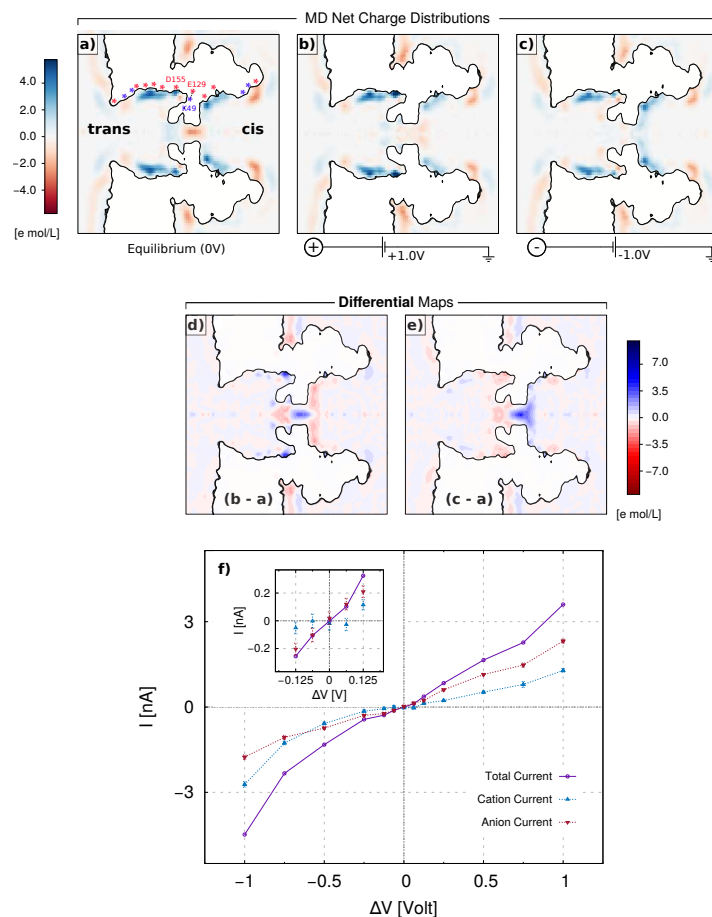
**Supplementary Figure S10. Ionic currents for the model system** shown in Fig. 1d-f and Fig. 3a-c of the manuscript. Currents are computed with the protocol described in the methods, averaging over 800 ns MD trajectories, for a total of 16 000 frames. The first 30 ns are discarded. Errors are smaller than the point sizes and are calculated using a block average protocol with a block length of 10 ns. It is apparent that for low voltages,  $|\Delta V| \leq 0.125$  V, the anion and cation currents are equal (see the inset). This is expected since, at low  $\Delta V$ , the external voltage does not alter the equilibrium ionic distributions. Since the pore surface is neutral and the salt is symmetric, the distributions of anions and cations are identical at equilibrium. Moreover, in our model anion and cations have the same mobility, consequently the anion and cation currents have the same value.



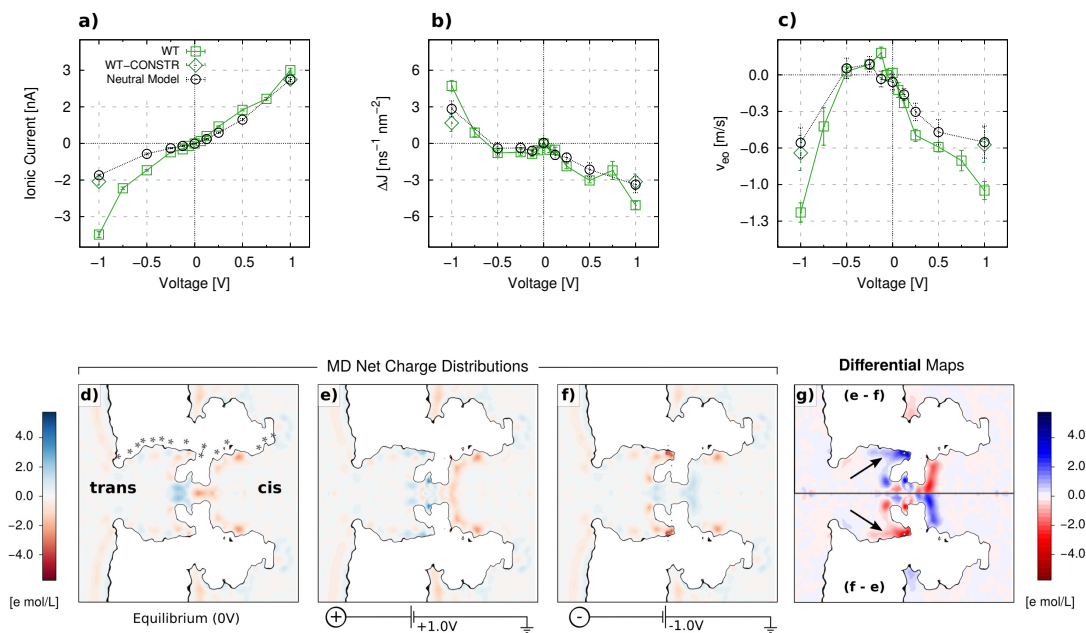
**Supplementary Figure S11. Electric Potential and Field lines for different cavity size.** The white arrowed lines represent the electric field  $\mathbf{E}(r, z) = -\nabla V$ . We filtered out the lines where  $|\mathbf{E}(r, z)| < 15\%$  of the maximum intensity. The potential map is averaged over 800 ns MD trajectory (16 000 frames), at  $\Delta V = +0.75 \text{ V}$  transmembrane applied bias, in presence of the model symmetric electrolyte. For the top group, the other geometric parameters are those of Fig. 3a-c of the manuscript, namely,  $R = 10 \text{ \AA}$ ,  $L = 30 \text{ \AA}$ ,  $s = 9 \text{ \AA}$ ,  $w = 12 \text{ \AA}$ . For the bottom group the geometric parameters are those of Fig. 3f, namely  $R = 14 \text{ \AA}$ ,  $L = 18 \text{ \AA}$ ,  $h = 5 \text{ \AA}$ ,  $w = 12 \text{ \AA}$ . The intensity of the electric field is larger in the solid region close to the cavity (where the membrane thickness is smaller) accordingly with the model already reported in Supplementary Note S1. It can be noted that the flux of the radial component of the electric field normal to the pore wall  $E_r(R, z)$ , increases as the cavity depth  $d$  increases and as the coaxial separating membrane thickness  $s$  decreases (both for fixed  $L$ ).



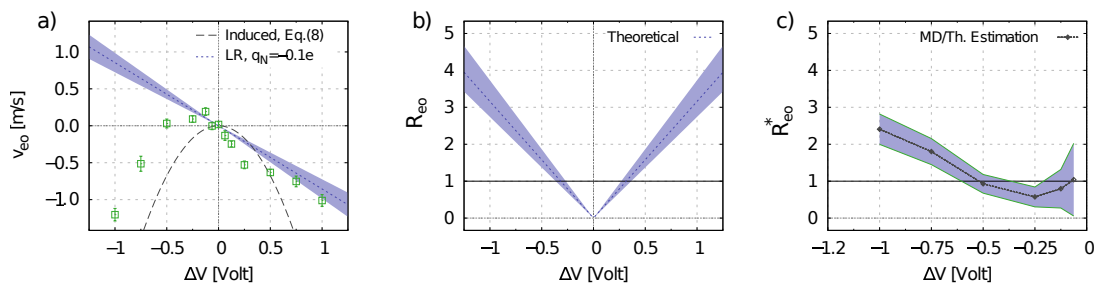
**Supplementary Figure S12. EOF predictions for a silicon nitride nanopore.** We considered a pore of radius  $R = 20$  nm and length  $L = 20$  nm. The lateral cavity has a depth  $d = 10$  nm and it is placed at a distance  $s = 40$  nm ( $s/R = 2$ ),  $s = 20$  nm ( $s/R = 1$ ) and  $s = 10$  nm ( $s/R = 0.5$ ). The relative electrical permittivity for solid and liquid are  $\epsilon_S = 7.5$  (silicon nitride) and  $\epsilon_L = 80$  (water). Panels represent different electrolyte concentration: **a)** 2 M, **b)** 0.2 M and **c)** 0.02 M. The corresponding Debye lengths  $\lambda_D$  are also reported on the top of each panel. The parabolic unidirectional EOF is obtained using Eq. (8) of the manuscript.



**Supplementary Figure S13. Net charge distribution and ionic currents for the CsgG nanopore,** Fig. 5 of the main text, computed from MD simulations in 2M KCl water solution. The first three panels (a-c) contain the maps already reported in Fig. 5b-c. Panels d-e, instead, represent the differential maps between the non-equilibrium systems ( $\Delta V = +1$  V, panels b and c) and the equilibrium one ( $\Delta V = 0$  V). The black line delimiting the pore and the membrane is the water density contour level  $\rho = 0.5\rho_{bulk}$ , with  $\rho_{bulk}$  the bulk water density. Maps are obtained from 280 ns MD production runs. All the trajectories are sampled each 20 ps, and analyzed discarding the first 10 ns. The applied  $\Delta V$  results in a strong reduction of the dipole in the pore constriction observed at  $\Delta V = 0$ , for this reason, the differential maps (c - a) and (b - a) present a dipole in the constriction. In the differential maps, it is also apparent that the cavity changes its charge when reverting the voltage. In particular at  $\Delta V = 1$  V differential maps (d) shows a positive variation of the cavity charge while the opposite occurs at  $\Delta V = -1$  V (e). Panel f reports the total electric current and single ionic currents. Currents and maps are computed with the protocols described in the methods, averaging over 280 ns MD production trajectories. for a total of 14000 frames. All the trajectories are sampled each 20 ps, and the first 10 ns are discarded. Errors are calculated using a block average protocol with a block length of 10 ns.



**Supplementary Figure S14. Comparison between the CsgG nanopore, Fig. 5 of the manuscript, and a Neutral Model of the same pore.** The Neutral Model is obtained by neutralizing the net charges of the acidic and basic residues, using standard neutral CHARMM patches of the charged residues. MD simulation are conducted in 2 M KCl water solution, as for Fig. 5. The general trends for **a)** ionic currents, **b)** selectivity and **c)** electroosmotic velocity are similar to the Wild Type CsgG nanopore. The quantitative differences in the fluxes at high voltages are due to slight structural changes of the constriction. To prove this, we repeated the simulation of the wild type CsgG by keeping the structure constrained upon the Neutral Model. The results, green diamond points (WT-CONST) at  $\Delta V = \pm 1.0V$ , overlap with Neutral Models. Currents are computed with the protocol described in the methods. Each point is obtained by averaging over 240 ns MD trajectory, for a total of 120 000 frames. The first 10 ns are discarded. Errors are calculated using a block average protocol with a block length of 10 ns. Panels **d-g** report the charge density map for the Neutral Model. Charge distribution at the walls of cis and trans vestibule differs from the Wild Type (Fig. 5.b-c of the manuscript). This is expected since the exposed residues that were originally charged in the Wild Type are now neutral. Instead, the charge distribution in the constriction is only slightly altered with respect to the Wild Type.



**Supplementary Figure S15. Comparison between Induced Charge EOF and Intrinsic Selectivity EOF for the CsgG nanopore.** To estimate the relative contribution of our geometrically induced mechanism on observed EOF we applied a simple additive model. **a)** Electroosmotic average velocity  $v_{eo}$  as a function of the applied voltage  $\Delta V$ . Green squared points and dashed grey line are the MD data and theoretical prediction of the geometrically induced charge model as reported in Fig. 5. The LR linear curve is obtained from Eqs. (5-6) of the manuscript, considering a fixed  $q_N = -0.10 \pm 0.015e$  inside the pore lumen. **b)** Ratio  $R_{eo}$  between the theoretical induced charge contribution  $v_{eo,ICEO}$  (dashed parabola in panel **a**) and the intrinsic linear  $v_{eo,LR}$  contribution to EOF (dotted line in panel **a**),

$$R_{eo} = \frac{|v_{eo,ICEO}|}{|v_{eo,LR}|}.$$

**c)** Ratio  $R_{eo}^*$  between the estimated induced charge contribution  $v_{eo,ICEO}^*$  and  $v_{eo,LR}$ , where  $v_{eo,ICEO}^*$  is computed at each  $\Delta V$  as the difference between the MD measured EOF and the LR value,  $v_{eo,ICEO}^* = v_{eo,MD} - v_{eo,LR}$ . This expression, as well as the overall analysis discussed in this supplementary figure, implicitly assumes a superimposition of effects, *i.e.* the total EOF can be decomposed as the sum of a linear contribution due to intrinsic selectivity and a quadratic contribution due to induced charge. This hypothesis is quite strong and, in general, unjustified. Consequently, these arguments can be used to get preliminary approximate voltage ranges where the intrinsic selectivity or the induced charge mechanism dominate the EOF, while simulations are needed for a reliable non-equilibrium description of the transport.

## SUPPLEMENTARY REFERENCES

- [S1] P. Läuger, W. Lesslauer, E. Marti, and J. Richter, *Biochimica et Biophysica Acta (BBA)-Biomembranes* **135**, 20 (1967).
- [S2] R. B. Schoch, J. Han, and P. Renaud, *Reviews of modern physics* **80**, 839 (2008).
- [S3] H. Bruus, *Theoretical microfluidics* (Oxford university press Oxford, 2008).
- [S4] M. Chinappi and F. Cecconi, *Journal of Physics: Condensed Matter* **30**, 204002 (2018).
- [S5] E. L. Bonome, F. Cecconi, and M. Chinappi, *Microfluidics and Nanofluidics* **21**, 96 (2017).
- [S6] K. Willems, D. Ruić, F. L. Lucas, U. Barman, N. Verellen, J. Hofkens, G. Maglia, and P. Van Dorpe, *Nanoscale* **12**, 16775 (2020).
- [S7] J. Wilson, K. Sarthak, W. Si, L. Gao, and A. Aksimentiev, *ACS sensors* **4**, 634 (2019).
- [S8] W. Humphrey, A. Dalke, and K. Schulten, *Journal of molecular graphics* **14**, 33 (1996).
- [S9] P. Virtanen, R. Gommers, T. E. Oliphant, M. Haberland, T. Reddy, D. Cournapeau, E. Burovski, P. Peterson, W. Weckesser, J. Bright, S. J. van der Walt, M. Brett, J. Wilson, K. Jarrod Millman, N. Mayorov, A. R. J. Nelson, E. Jones, R. Kern, E. Larson, C. Carey, Í. Polat, Y. Feng, E. W. Moore, J. Vand erPlas, D. Laxalde, J. Perktold, R. Cimrman, I. Henriksen, E. A. Quintero, C. R. Harris, A. M. Archibald, A. H. Ribeiro, F. Pedregosa, P. van Mulbregt, and S. . . Contributors, *Nature Methods* **17**, 261 (2020).
- [S10] J. D. Hunter, *Computing in Science & Engineering* **9**, 90 (2007).
- [S11] D. J. Bonthuis, S. Gekle, and R. R. Netz, *Physical review letters* **107**, 166102 (2011).
- [S12] G. Raabe and R. J. Sadus, *The Journal of chemical physics* **134**, 234501 (2011).
- [S13] J. H. Weijs, A. Marchand, B. Andreotti, D. Lohse, and J. H. Snoeijer, *Physics of fluids* **23**, 022001 (2011).
- [S14] D. Frenkel and B. Smit, *Understanding molecular simulation: from algorithms to applications*, Vol. 1 (Elsevier, 2001).
- [S15] P. Atkins and J. De Paula, *Physical chemistry for the life sciences* (Oxford University Press, USA, 2011).